DYNAMIC BIPEDAL WALKING UNDER STICK-SLIP TRANSITIONS*

BENNY GAMUS AND YIZHAR OR†

Abstract. This paper studies the hybrid dynamics of bipedal robot walking under stick-slip transitions. We focus on two simple planar models with point feet: the rimless wheel and the compass biped. Unlike most of existing works in the literature that assume sticking contact between the foot and the ground, we explore the case of insufficient friction which may induce foot slippage. Numerical simulations of passive dynamic walking reveal the onset of stable periodic solutions involving stick-slip transitions. In the case of the compass biped with controlled joint torques actuation, we demonstrate how one can exploit kinematic trajectories of passive walking in order to induce and stabilize gaits with slipping impact.

1. Introduction. Legged locomotion is ubiquitous in living creatures across a wide range of scales, from tiny insects through lizards and rodents up to humans and large mammals [20]. Inspired by this natural mode of locomotion, many legged robots have been developed, such as humanoids [36, 40], quadrupedal robots [42, 51], hexapedal robots [7, 65], and even hybrid wheeled/tracked/legged vehicles [70]. Such mobile robots are intended to be used mainly for negotiating unstructured terrains or indoor environments where traditional wheeled and tracked vehicles have limited maneuverability or accessibility. Potential applications of autonomous legged robots vary from military and security [62] through search and rescue [42] to education and entertainment [2, 77], rehabilitation assistance [1, 21], and even planetary exploration [44, 84]. Unlike quasistatic locomotion, in which the robot moves slowly through a sequence of equilibrium postures [63, 56], in dynamic legged locomotion (DLL) the robot constantly undergoes unsteady motion of falling, followed by placement of a free foot on the ground and transfer of the support, typically in a cyclic pattern called *gait*.

Theoretical investigation of DLL has been subject to extensive research efforts in the fields of theoretical mechanics, biomechanics, robotics, and nonlinear control, cf. [31, 38, 82]. Some of these works are inspired by biological locomotion of insects and large animals [24, 37], e.g. the well-known RHex robot [65], for which the legs' elasticity plays a major role. On the other hand, for legged robots with rigid links, foot-ground contact is established via impact events which involve discontinuous momentum changes, giving rise to a hybrid dynamical system with nonsmooth behavior [5, 10, 28]. One of the most classical and simple models of DLL is McGeer's passive bipedal walker [48] which is a two-link robot that walks stably down a shallow slope, powered solely by gravity. The passive dynamics of this two-link model, named *compass biped*, is further analyzed by Goswami in [29]. In his work [48], McGeer also introduces and analyzes an even simpler and low-dimensional model - the *rimless spoked wheel*, which is further analyzed by Coleman and Ruina [15, 14].

A central theme in the analysis of DLL is orbital stability of hybrid periodic solutions, which can be assessed via linearization of the Poincaré map [34]. Stability can be achieved either passively as in [15, 14, 29, 48], or by using active feedback

*This research has been supported in part by the Arlene & Arnold Goldstein Center at the Technion's Autonomous Systems Program (TASP) under grant no. 2015136. A short and preliminary version of this work has been published in the Proceedings of 2013 IEEE International Conference on Robotics and Automation (ICRA 2013) [25].

†Faculty of Mechanical Engineering, Technion - Israel Institute of Technology, Haifa 32000, Israel (izi@tx.technion.ac.il).

control of the motor torques at the robot's joints according to sensory information [35, 38, 82]. Feedback control of DLL has been a highly active field of research in the last decade. Focusing on bipedal robots, sophisticated nonlinear techniques have been recently employed, with emphasis on advanced geometric notions such as controlled symmetries [73], Routhian reduction [30], hybrid zero dynamics [83], transverse linearization [23] and virtual holonomic constraints [18]. Another important concept in controlled legged locomotion is energetic efficiency [46, 69]. Many works attempt to minimize the *specific cost of walking* – the mechanical work expended (on average) by the controlled actuators per forward distance [26, 45, 64]. Development of control laws which are based on gaits of passive dynamics has been proven to be a successful approach for finding energy-efficient gaits [16, 74]. These gaits exploit the robot's passive dynamics and thus require only a small amount of actuation power.

A key limitation of almost all theoretical models which are used for investigation of legged locomotion as mentioned above is that they assume that the foot-ground contact is a stationary pivot point, and that no foot slippage occurs throughout the motion and during impacts. This assumption is not always physically realistic, since it requires that friction at the foot-ground contact is sufficiently large in order to enforce sticking. Moreover, perturbations caused by external forces, vibrations, or local changes in the surface properties can impose foot slippage even for large friction.

In biological legged locomotion, it has already been observed that slippage has a prominent influence across all macroscopic scales. At the length scale of millimeters, weaver ants have evolved several adhesive mechanisms in order to overcome slippage on the lubricated surface of pitcher plants [9]. Stick insects confronted with a slippery surface modulate their motor outputs to produce normal walking gaits, despite a drastic change in the loads that these limbs experience [32, 33]. In the centimeter scale, the elephant shrew is remarkable in constructing known escape routes in loose, slippery dirt [71]. Clark et al [13] studied slippage in running Guinea fowl, showing that falling on slippery surfaces is a strong function of both speed and limb posture at touchdown. In the scale of meters, the largest body of work on slipping is on human biomechanics. The conditions that cause slipping [50], its consequences [49] and dynamics [75] have been studied, with important applications in preventative care for the elderly, shoe design, safety, and more.

In the legged robotics literature, few works incorporate friction considerations in designing gaits that avoid slippage [11, 39], and some works studied detection and estimation of slippage from sensory data [41, 80].

In physics and computer-graphics simulators of multibody systems and biomechanical models such as Bullet Physics and OpenSim [68, 19], unilateral contact is often modeled as an array of discrete nodes with nonlinear springs and dampers. This model typically results in a complex high-dimensional system of differential equations whose solution is commonly very stiff due to combination of small deformations at the contact nodes and large motions of links far from contact. Moreover, physical values such as spring constants and nonlinear friction forces are often chosen arbitrarily without any justification from a mechanical model or experiment. On the other hand, Coulomb's law of dry friction [17, 60] provides a well-established simple contact model for low-dimensional systems of multibody dynamics. Despite the evident importance of foot slippage, theoretical study of legged locomotion dynamics under possible stick-slip transitions using Coulomb's friction model has rarely been considered, except for the works [6, 78, 79, 85].

The goal of this paper is to bridge this gap by studying simple models of bipedal

dynamic walking that involve stick-slip transitions at the feet under Coulomb's dry friction model and analyzing the effect of foot slippage on the behavior and performance of dynamic walking, both passive and actuated. The paper studies the models of rimless spoked wheel and compass biped under passive dynamics on a slope, and also the controlled torque-actuated compass biped on a horizontal plane. It is found that when the friction is not sufficient to maintain contact sticking, the solution evolves towards periodic cycles (gaits) that involve foot slippage and stick-slip transitions, which maintain orbital stability with a slowr rate of convergence. In the case of a torque-actuated compass biped model, it is shown that gaits which involve slipping impacts have improved energetic efficiency compared to contact-sticking gaits. Such gaits which are open-loop unstable can be easily stabilized via simple feedback control. It is concluded that foot slippage effects can have a substantial influence on both passive and actuated dynamic walking.

The structure of the paper is as follows. The next section gives a general formulation of the equations of motion. Section 3 studies the rimless spoked wheel, Section 4 studies the passive compass biped on a slope, and Section 5 studies the torque-actuated compass biped on a horizontal plane. Finally, Section 6 concludes and discusses some possible directions of future extension. A concluding discussion is given in the closing section. Finally, two appendices give detailed formulation of the dynamics and provide a detailed proof of one technical statement.

2. Problem Formulation. This section gives a brief overview of the formulation of the hybrid dynamics of planar biped robots with point feet that walk on a flat surface, which is used throughout the paper. Some of the technical details and derivations are relegated to Appendix A. The robot model is either a single rigid body or a kinematic chain of rigid links. A particular material point on the robot, which is called the *stance foot*, is maintaining contact with the ground. Another material point which is called the *swing foot*, is currently detached from the ground and is supposed to establish contact at the next step. When the swing foot hits the ground the stance foot detaches, and the feet switch roles for the next step. The hybrid dynamics is composed of two phases which are formulated below — a continuous-time phase during which the swing foot moves forward, and an instantaneous impact phase, caused by collision of the swing foot with the ground.

2.1. Continuous-time dynamics. Let $\mathbf{q} \in \mathbb{R}^N$ denote the coordinates which describe the position of each of the robot's links. In particular, the coordinates $\mathbf{q}$ describe the position $\mathbf{r}$ of the stance foot, and its velocity vector $\dot{\mathbf{r}}$ depends on both positions $\mathbf{q}$ and velocities $\dot{\mathbf{q}}$. Let v_t and v_n denote the components of the stance foot's velocity $\dot{\mathbf{r}}$ in the directions tangent and normal to the surface. These components can be formulated as

$$v_t = \mathbf{w}_t(\mathbf{q}) \cdot \dot{\mathbf{q}} \ , \ v_n = \mathbf{w}_n(\mathbf{q}) \cdot \dot{\mathbf{q}}. \tag{1}$$

When the foot maintains a sticking contact with the ground, both v_t and v_n vanish. In case where the foot is slipping $v_t \neq 0$, only the constraint on the normal velocity $\mathbf{w}_n(\mathbf{q}) \cdot \dot{\mathbf{q}} = 0$ holds. The equations of motion of the robot can be formulated using the method of constrained Lagrange's equations (cf. [52]), and are given by

$$\mathbf{M}(\mathbf{q})\ddot{\mathbf{q}} + \mathbf{B}(\mathbf{q}, \dot{\mathbf{q}}) + \mathbf{G}(\mathbf{q}) = \mathbf{E}(\mathbf{q})\mathbf{u}(t) + \mathbf{W}(\mathbf{q})^T\mathbf{f} \tag{2}$$

where $\mathbf{M}(\mathbf{q})$ is called the matrix of inertia, $\mathbf{B}(\mathbf{q}, \dot{\mathbf{q}})$ is the vector of velocity-dependent terms such as Coriolis and centripetal forces, and the vector $\mathbf{G}(\mathbf{q})$ contains gravitational forces. On the right hand side of (2), the vector $\mathbf{u}(t) \in \mathbb{R}^m$ augments the

controlled torques at actuated joints (if they exist), where $\mathbf{E}(\mathbf{q})$ maps these torques to their associated generalized forces. The matrix $\mathbf{W}(\mathbf{q}) = [\mathbf{w}_t(\mathbf{q}) \;\; \mathbf{w}_n(\mathbf{q})]^T$ is the robot's Jacobian matrix with respect to the stance foot's position, i.e. $\mathbf{W}(\mathbf{q}) = d\mathbf{r}/d\mathbf{q}$. The vector $\mathbf{f} = [f_t \;\; f_n]^T$ contains the tangential and normal components of the contact force acting at the stance foot. Assuming Coulomb's dry friction model [17], these components must satisfy the inequality given by

$$|f_t| \leq \mu f_n, \tag{3}$$

where $\mu \geq 0$ is the coefficient of friction, which is assumed to be a given property of the surfaces in contact. When inequality (3) is not satisfied, tangential slippage of the contact point starts to evolve, i.e. $v_t \neq 0$. In that case, according to Coulomb's friction model, the tangential contact force f_t opposes the direction of slippage, and depends on the normal force f_n as $f_t = -\text{sgn}(v_t)\mu f_n$. (For simplicity, we do not distinguish between static and kinetic friction throughout this work). Thus, the contact force $\mathbf{f}$ is a function of positions $\mathbf{q}$ and velocities $\dot{\mathbf{q}}$, and depends on the instantaneous state of the contact — sticking or slipping. This distinction is the main difference between our work and vast majority of the works on dynamic biped locomotion in the literature, which always assume sticking contact. A detailed derivation of the expressions for the contact force is given in Appendix A.

The dynamics in (2) can also be written as a state equation, which is a first-order vector differential equation. The state vector of the system combines the robot's positions and velocities $\mathbf{x} = (\mathbf{q}, \dot{\mathbf{q}}) \in \mathbb{R}^{2N}$. The state equation can then be written in the form $\dot{\mathbf{x}} = \mathcal{F}(\mathbf{x}, \mathbf{u})$, as detailed in Appendix A. Alternative ways to formulate the equations of motion for this class of unilaterally constrained mechanical systems are by using complementarity [3, 60] or convex analysis formulation [61], which are not discussed here.

2.2. Impact law. We now formulate the impact interaction that occurs when the swing foot collides with the ground. The assumption of perfectly rigid bodies implies that a collision results in an instantaneous change in the velocities which is caused by impulsive contact forces. Let $\tilde{\mathbf{r}}$ denote the swing foot's position during motion, and let $\tilde{\mathbf{W}}(\mathbf{q}) = d\tilde{\mathbf{r}}/d\mathbf{q}$ be its Jacobian matrix. At the time $t{=}t_c$, the swing foot $\tilde{\mathbf{r}}$ hits the ground, and an impact occurs. The impact process involves a very short contact interaction where a large contact force $\tilde{\mathbf{f}}(t)$ acts at the colliding foot and causes an instantaneous change in the velocities $\dot{\mathbf{q}}$. It is assumed that the coordinates $\mathbf{q}$ remain unchanged during the impact process $\mathbf{q}(t = t_c) = \mathbf{q}_c$. The change in the velocities $\dot{\mathbf{q}}$ is governed by impulse-momentum balance as

$$\mathbf{M}_c \left(\dot{\mathbf{q}}(t_c^+) - \dot{\mathbf{q}}(t_c^-)\right) = \tilde{\mathbf{W}}_c^T \tilde{\mathbf{F}}, \tag{4}$$

where the contact impulse $\tilde{\mathbf{F}}$ is the time-integral of the contact force $\tilde{\mathbf{f}}$ during the short time of collision, i.e. $\tilde{\mathbf{F}} = \int \tilde{\mathbf{f}}(t)dt$. The superscripts '+' and '−' in (4) denote the time right after and right before the collision, and $\mathbf{M}_c$ and $\mathbf{W}_c$ are shorthand notations for $\mathbf{M}(\mathbf{q}{=}\mathbf{q}_c)$ and $\mathbf{W}(\mathbf{q}{=}\mathbf{q}_c)$, respectively.

In the literature on legged robots, is it is almost always assumed that collisions are perfectly plastic, so that the impact results in sticking contact at the colliding foot. However, incorporating Coulomb's friction model implies that the tangential and normal components of the contact impulse $\tilde{\mathbf{F}}$ must satisfy the inequality

$$\left|\tilde{F}_t\right| \leq \mu \tilde{F}_n. \tag{5}$$

If a plastic collision cannot be obtained while satisfying the inequality (5), the impact must result in slippage while the tangential impulse attains its maximal allowed magnitude $\tilde{F}_t = \pm\mu\tilde{F}_n$. The process described above gives rise to an impact law, which describes the changes in the velocities due to impact. This relation, which is linear in velocities $\dot{\mathbf{q}}$ and nonlinear in configuration $\mathbf{q}$, is given by $\dot{\mathbf{q}}^+ = \boldsymbol{\beta}(\mathbf{q}_c)\dot{\mathbf{q}}^-$, where $\dot{\mathbf{q}}_c^+$ and $\dot{\mathbf{q}}_c^-$ are shorthand notations to $\dot{\mathbf{q}}(t = t_c^+)$ and $\dot{\mathbf{q}}(t = t_c^-)$, respectively. Detailed derivation of the matrix $\boldsymbol{\beta}(\mathbf{q}_c)$ is given in Appendix A.

In models of biped locomotion, the impact is typically followed by relabeling of the coordinates in order to account for the switch in the roles of the feet. This is commonly done by applying linear transformations to the positions and velocities $\mathbf{q} \to \mathbf{S}_1\mathbf{q}$ and $\dot{\mathbf{q}} \to \mathbf{S}_2\dot{\mathbf{q}}$ where $\mathbf{S}_1$ and $\mathbf{S}_2$ are constant $N \times N$ matrices. In state-space formulation, composition of the coordinates relabeling with the impact law can be expressed as a linear relation between the pre-impact and post-impact values as

$$\mathbf{x}^+ = \mathcal{X}(\mathbf{x}_c)\mathbf{x}^-, \quad \text{where } \mathcal{X}(\mathbf{x}_c) = \begin{pmatrix} \mathbf{S}_1 & 0 \\ 0 & \mathbf{S}_2\boldsymbol{\beta}(\mathbf{q}_c) \end{pmatrix}. \tag{6}$$

2.3. Hybrid dynamics and solutions. We now define the hybrid dynamics of the system, which consists of a concatenation of continuous-time phases interleaved with discrete impact events. First, we define the sets of double-contact configurations in state space (i.e. where the two feet touch the ground), as follows. Let $\tilde{r}_n(\mathbf{q})$ be the normal distance of the swing foot from the ground, and let $v_n = \dot{\tilde{r}}_n$ denote the swing foot's normal velocity. The sets of double-contact pre-impact and post-impact states are defined as

$$\begin{aligned} \Sigma^- &= \{(\mathbf{q}, \dot{\mathbf{q}}) : \quad \tilde{r}_n(\mathbf{q}) = 0 \text{ and } \tilde{v}_n(\mathbf{q}, \dot{\mathbf{q}}) < 0\} \\ \Sigma^+ &= \{(\mathbf{q}, \dot{\mathbf{q}}) : \quad \tilde{r}_n(\mathbf{q}) = 0 \text{ and } \tilde{v}_n(\mathbf{q}, \dot{\mathbf{q}}) > 0\}. \end{aligned} \tag{7}$$

Using the standard formulation of [28], the hybrid dynamics of the robot can then be represented as the combination of a differential equation and a discrete jump as

$$\begin{cases} \dot{\mathbf{x}}(t) = \mathcal{F}(\mathbf{x}, \mathbf{u}) & \mathbf{x}(t) \notin \Sigma^- \\ \mathbf{x}(t^+) = \mathcal{X}(\mathbf{x})\mathbf{x}(t^-) & \mathbf{x}(t^-) \in \Sigma^- \end{cases} \tag{8}$$

Note that both $\mathcal{F}(\mathbf{x}, \mathbf{u})$ and $\mathcal{X}(\mathbf{x})$ in (8) are piecewise smooth, due to the stick/slip conditions, see Appendix A. A solution of the hybrid dynamics (8) under given initial condition $\mathbf{x}(0)$ and control input $\mathbf{u}(t)$ consists of an ordered set of impact times $\Upsilon = \{t_1, t_2, \ldots\}$ and a piecewise-continuous time-dependent vector $\mathbf{x}(t)$ which satisfies $\dot{\mathbf{x}}(t) = \mathcal{F}(\mathbf{x}(t), \mathbf{u}(t))$ for all $t \notin \Upsilon$. At the discontinuity points $t_k \in \Upsilon$, the solution of $\mathbf{x}(t)$ satisfies the impact law $\mathbf{x}(t_k^+) = \mathcal{X}(\mathbf{x}(t_k^-))\mathbf{x}(t_k^-)$.

It is important to note that for hybrid systems which represent this particular class of mechanical systems with unilateral constraints (cf. [10, 61]), there exist special scenarios for which the solution may be inconsistent or non-unique due to the definition of stick/slip contact transitions. These cases, which are associated with the well-known paradox of Painlevé [47, 57, 59], are not considered in this work, since the paradox can only occur for very extreme values of physical parameters in the particular models considered here, see [54] for detailed analysis. Another phenomenon which is unique to hybrid systems is Zeno behavior [55, 58, 86], where the solution undergoes an infinite number of discrete transitions (impacts) in finite time. While Zeno behavior is typical to systems with rebound after impacts such as the classical bouncing ball problem (cf. [34]), it is much less relevant in the models considered here where completely plastic impacts with no rebound are assumed.

2.4. Hybrid periodic solutions and orbital stability. Since dynamic walking naturally involves periodic motion under hybrid dynamics, we now briefly discuss hybrid periodic solutions and their stability. A more detailed formalization can be found in [34, 82]. First, we introduce the (post-impact) Poincaré map of the hybrid dynamics. This is a map $\Pi : \Sigma^+ \to \Sigma^+$ which maps an initial post-impact state $\mathbf{x}_0 \in \Sigma^+$ to the post-impact state right after the next impact. The formal definition of Π is given by

$$\Pi(\mathbf{x}_0) = \mathbf{x}(t_c^+) = \mathcal{X}(\mathbf{x}(t_c^-))\mathbf{x}(t_c^-), \text{ where } t_c^- = \min\{t > 0 : \mathbf{x}(t) \in \Sigma^-\} \tag{9}$$

such that $\mathbf{x}(t)$ is the solution of (34) under initial condition $\mathbf{x}(0) = \mathbf{x}_0$. The domain Σ^+ of Π is called the (post-impact) Poincaré section. Note that not all solutions of (34) necessarily reach impact states at Σ^-, hence the map Π may be defined only on a subset of the Poincaré section Σ^+. The Poincaré map induces a discrete-time dynamical system which governs the step-to-step transition of a hybrid solution, as

$$\mathbf{x}_{k+1} = \Pi(\mathbf{x}_k) \tag{10}$$

where $\mathbf{x}_k = \mathbf{x}(t_k^+)$ is the series of post-impact states, i.e. right after the impacts. A fixed point $\mathbf{x}^*$ of (10) which satisfies $\Pi(\mathbf{x}^*) = \mathbf{x}^*$ corresponds to initial condition of a periodic solution of the hybrid system. For a bipedal robot model, $\mathbf{x}^*$ is precisely an initial condition which results in periodic motion of cyclic walking. The periodic solution is orbitally (asymptotically) stable if the corresponding fixed point $\mathbf{x}^*$ is (asymptotically) stable under the discrete-time dynamics (10). (See [34, 82] for more formal definitions of orbital stability). According to classical stability theory (cf. [43]), stability of $\mathbf{x}^*$ is determined by the eigenvalues of the linearization matrix $\mathbf{A} = \left.\dfrac{d\Pi}{d\mathbf{x}}\right|_{\mathbf{x}=\mathbf{x}^*}$ as follows: $\mathbf{x}^*$ is asymptotically stable if and only if all eigenvalues λ_i of $\mathbf{A}$ lie within the unit disc in the complex plane, i.e. they must satisfy $|\lambda_i| < 1$. Note that in most cases the Poincaré map Π, its fixed point $\mathbf{x}^*$ and the linearization matrix $\mathbf{A}$ can only be computed numerically. Only in very few low-dimensional cases these expressions can be found analytically, as in [27] and in [14, 48] which are also reviewed in the next section. Another important observation is that since Σ^+ is of dimension $2N-1$, the matrix $\mathbf{A}$ can be reduced to dimensions $(2N-1)\times(2N-1)$ when expressed in a suitable $(2N-1)$-dimensional parametrization of Σ^+. Moreover, in legged locomotion along a flat plane the dynamics is always independent of the coordinate associated with forward motion (i.e. in the notation of the next sections, x is a cyclic coordinate) so that this coordinate is ignored in Π as well, resulting in further reduction to dimension $2N-2$. (Formally, this notion is called restricted Poincaré map, see [82]). Note, however, that even though x is a cyclic coordinate, the stride length along a periodic solution, given by $\Delta x{=}x(t_{k+1}){-}x(t_k)$, is important.

3. Passive dynamics of the rimless wheel. This section studies the dynamics of the rimless wheel model (RW). The rimless wheel is a star-like rigid body with $n \geq 4$ evenly-spaced spokes, that rolls passively down an inclined plane in a way that resembles bipedal walking (see Figure 3.1(a)). At each time a single spoke is in contact with the ground and represents the stance foot, until the next spoke, which represents the swing foot, hits the ground and makes contact while the previous spoke is released. In what follows, known results from [14, 48] on the rimless wheel's dynamics under contact sticking are reviewed first. Then, constraints on the contact forces are studied and the dynamics under stick-slip transitions is analyzed, followed by delineation of regions of attraction of stable periodic solutions.

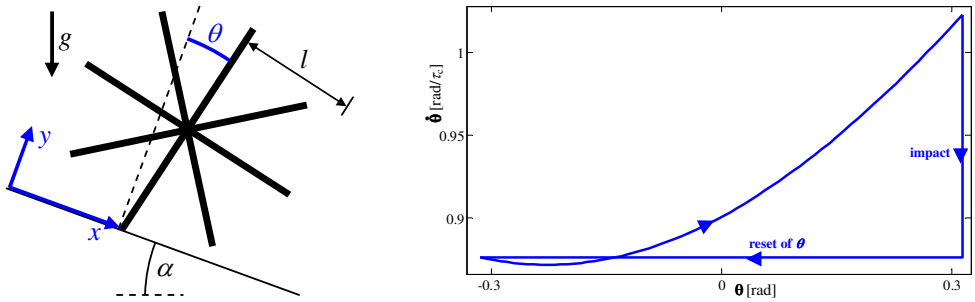

FIG. 3.1. *(a) The rimless wheel (RW) model. (b) Trajectory of periodic solution of the RW in* $(\theta, \dot{\theta})$*-plane under sticking contact (Type A solution) for* $\mu > \mu_c$.

We begin by formulating the equations of motion of the RW using the notation introduced in Section 2. Let m and I_c denote the wheel's mass and moment of inertia with respect to its center-of-mass, and let l denote the spokes' length. The gravity acceleration is denoted by g, and the slope angle of the inclined plane is α. The chosen coordinates are $\mathbf{q} = (x, y, \theta)$, where x and y denote the position of the contacting spoke's tip in the directions tangent and normal to the ground. Note that this position is constrained, such that $\dot{y} = 0$ means that the wheel maintains contact with the ground, while $\dot{x} = 0$ holds when the contact point does not slip. The third coordinate θ is the orientation angle of the contacting spoke with respect to the normal direction (y-axis, see Figure 3.1(a)). Thus, θ changes within the range $[-\pi/n, \pi/n]$ between two consecutive "steps", and after an impact at $\theta = \pi/n$ it is reset back to $-\pi/n$ for the next step. The kinetic and potential energies of the wheel are given by equation (41) in Appendix A. The continuous-time equations of motion can be derived in the form (2), and the impulse-momentum relation is of the form (4) where the expressions in these two equations are given as

$$\mathbf{M}(\mathbf{q}) = \begin{pmatrix} m & 0 & ml\cos\theta \\ 0 & m & -ml\sin\theta \\ ml\cos\theta & -ml\sin\theta & ml^2(1+\kappa) \end{pmatrix}, \quad \mathbf{B}(\mathbf{q},\dot{\mathbf{q}}) = \begin{pmatrix} -ml\dot{\theta}^2\sin\theta \\ -ml\dot{\theta}^2\cos\theta \\ 0 \end{pmatrix}, \quad \mathbf{Eu} = \begin{pmatrix} 0 \\ 0 \\ 0 \end{pmatrix}$$
$$\mathbf{G}(\mathbf{q}) = \begin{pmatrix} -mg\sin\alpha \\ mg\cos\alpha \\ -mgl\sin(\alpha+\theta) \end{pmatrix}, \quad \mathbf{W}(\mathbf{q}) = \begin{pmatrix} 1 & 0 & 0 \\ 0 & 1 & 0 \end{pmatrix}, \quad \tilde{\mathbf{W}}_c = \begin{pmatrix} 1 & 0 & 0 \\ 0 & 1 & -2l\sin\frac{\pi}{n} \end{pmatrix} \tag{11}$$

The nondimensional inertia ratio $\kappa{=}I_c/ml^2$ varies within the range $[0, 1]$, where $\kappa{=}0$ means that all the wheel's mass is concentrated at its center, $\kappa{=}1$ means that all the spokes' masses are concentrated at their tips, and $\kappa{=}1/3$ corresponds to uniform mass distribution along the spokes.

3.1. RW– Review of no-slip hybrid dynamics. We now briefly review known results on the hybrid dynamics of the RW model, which were derived in [14, 48] under the assumption of fully sticking contact. In particular, we discuss hybrid periodic solutions and their stability. Since the contact sticking constraint $\mathbf{W}(\mathbf{q})\dot{\mathbf{q}}{=}0$ simply implies that $\dot{x}{=}\dot{y}{=}0$, the equations of continuous-time motion in (2) with the expressions (11) reduce to the single equation for the angle θ:

$$\ddot{\theta} - \sin(\theta + \alpha) = 0. \tag{12}$$

Equation (12) is simply an inverted pendulum equation, where the time scale is normalized by the characteristic time $\tau_c = \sqrt{mgl/(ml^2 + I_c)}$. This equation is integrable

due to conservation of total mechanical energy. Thus, the angle θ and angular velocity $\dot{\theta}$ satisfy the relation

$$\dot{\theta}^2 = \dot{\theta}_0^2 + 2\cos\left(\alpha - \frac{\pi}{n}\right) - 2\cos\left(\alpha + \theta\right) \tag{13}$$

where $\theta(0) = -\pi/n$ and $\dot{\theta}_0 = \dot{\theta}(0)$ is the initial angular velocity. Impact occurs at $\theta = \pi/n$. Assuming sticking contact, the impact induces a discontinuous jump of the angular velocity $\dot{\theta}$ which can be obtained as (see (38) in Appendix A):

$$\dot{\theta}^+ = \beta\dot{\theta}^-, \text{ where } \beta = \frac{\cos(2\pi/n) + \kappa}{1 + \kappa}. \tag{14}$$

Denoting the state vector as $\mathbf{x} = (\theta, \dot{\theta})$, the post-impact Poincaré section is defined as $\Sigma^+ = \{(\theta, \dot{\theta}) : \ \theta = -\pi/n \text{ and } \dot{\theta} > 0\}$, which is parametrized by $\dot{\theta}$. Using the energy relation (13) and the impact law (14), the scalar Poincaré map which maps an initial post-impact angular velocity $\dot{\theta}_0$ to the velocity right after the next impact $\dot{\theta}_c^+$ is given by

$$\Pi(\dot{\theta}_0) = \dot{\theta}_c^+ = \beta\sqrt{\dot{\theta}_0^2 + 4\sin\alpha\sin(\pi/n)}. \tag{15}$$

The Poincaré map in (15) has a fixed point $\dot{\theta}^*$ satisfying $\Pi(\dot{\theta}^*) = \dot{\theta}^*$, which is given by

$$\dot{\theta}^* = 2\beta\sqrt{\frac{\sin\alpha\sin(\pi/n)}{1 - \beta^2}}. \tag{16}$$

This fixed point corresponds to a hybrid periodic solution of the RW dynamics. As an example, Figure 3.1(b) plots the closed-loop trajectory of the periodic solution in $(\theta, \dot{\theta})$-plane for parameter values of n=10, κ=1/3 and α=13°. The vertical line segment corresponds to the jump in $\dot{\theta}$ due to impact, while the horizontal line segment corresponds to re-initialization of θ from π/n back to $-\pi/n$. This periodic solution, which assumes sticking contact without foot slippage, is denoted as Type A and its animation can be found in the supplementary material [87]. Stability of this periodic solution is determined by the single eigenvalue of the linearization of Π about its fixed point, which is given by

$$\left.\frac{d\Pi}{d\dot{\theta}_0}\right|_{\dot{\theta}_0 = \dot{\theta}^*} = \beta^2 < 1. \tag{17}$$

Since the magnitude of this eigenvalue is less than unity, it is concluded that the periodic orbit associated with $\dot{\theta}^*$ is asymptotically stable.

It is important to note that the fixed point $\dot{\theta}^*$ as defined in (16) does not actually exist in all cases. This happens because the energy relation (13) which relates $\dot{\theta}$ to $\dot{\theta}_0^2$ does not capture the sign of $\dot{\theta}$, and thus may give a false prediction of a periodic solution in cases where $\dot{\theta}(t)$ becomes negative and $\theta(t)$ evolves backwards and do not reach the contact at $\theta = \pi/n$. This scenario is possible for shallow slopes $\alpha < \pi/n$ for which the upright equilibrium position $\theta = -\alpha$ lies within the range of feasible orientation angles $[-\pi/n, \pi/n]$. In such cases, one needs to verify that the initial kinetic energy of the wheel is large enough for crossing the upright equilibrium position where $\theta = -\alpha$. Substituting $\dot{\theta}_0 = \dot{\theta}^*$ from (16) and $\theta = -\alpha$ into (13), gives the inequalities

$$\frac{4\beta^2}{1 - \beta^2}\sin\alpha\sin\frac{\pi}{n} + 2\cos\left(\alpha - \frac{\pi}{n}\right) - 2 > 0, \text{ or } \alpha > \frac{\pi}{n}. \tag{18}$$

For given values of κ and n, this inequality implies a lower bound on the slope angle $\alpha > \alpha_{min}$. As an example, for parameter values n=10 and κ=1/3, the slope angle must satisfy $\alpha > 1.4^\circ$ in order to guarantee existence of the periodic solution for $\dot{\theta}_0 = \dot{\theta}^*$. (This comes from the first inequality in (18)).

3.2. RW– Constraints on contact forces. We now analyze the constraints on contact forces which were not considered in the works [15, 48] and [14]. Using the expressions in (11) the components of the contact force $\mathbf{f}$ under contact sticking are obtained from (31) as

$$\begin{aligned} f_n(\theta, \dot{\theta}) &= \tfrac{mg}{1+\kappa} \Big((\cos(\alpha+\theta) - \dot{\theta}^2) \cos\theta + \kappa \cos\alpha \Big) \\ f_t(\theta, \dot{\theta}) &= \tfrac{mg}{1+\kappa} \Big((\cos(\alpha+\theta) - \dot{\theta}^2) \sin\theta - \kappa \sin\alpha \Big) . \end{aligned} \tag{19}$$

In [48] and [14], the possibility of contact slippage is ignored, which is equivalent to assuming arbitrarily large friction coefficient μ, so that inequality (3) is always satisfied. Moreover, these works did not consider the requirement that the normal force f_n must be positive in order to maintain contact and avoid detachment. In order to check this requirement, the normal force f_n in (19) can be expressed in terms of θ and $\dot{\theta}_0$ only, by using the energy relation (13). Substituting the initial condition of a periodic solution $\dot{\theta}_0 = \dot{\theta}^*$, one obtains the normal contact force along a periodic solution as

$$f_n^*(\theta) = \frac{mg}{1+\kappa} \Big(\Big(3\cos(\alpha+\theta) - (\dot{\theta}^*)^2 - 2\cos(\alpha - \tfrac{\pi}{n}) \Big) \cos\theta + \kappa \cos\alpha \Big) . \tag{20}$$

For the range $\theta \in [\pi/n, \pi/n]$, it is proven in Appendix B that $f_n^*(\theta)$ always attains its minimum at $\theta = \pi/n$. Therefore, in order to maintain positive normal contact force along the entire periodic solution, the inequality $f_n^*(\theta = \pi/n) \geq 0$ must be satisfied. Substituting the expression for $\dot{\theta}^*$ from (16) into (20) then gives a scalar inequality in the parameters κ, α and n, as

$$\left(3\cos(\alpha + \tfrac{\pi}{n}) - 4\beta^2 \frac{\sin\alpha \sin(\pi/n)}{1-\beta^2} - 2\cos(\alpha - \tfrac{\pi}{n}) \right) \cos(\tfrac{\pi}{n}) + \kappa \cos\alpha > 0, \tag{21}$$

where $\beta = \beta(\kappa, n)$ is defined in (14). For given values of κ and n, inequality (21) imposes an upper bound on the slope angle $\alpha < \alpha_{max}$. For example, for parameter values n=10 and κ=1/3, the slope angle must satisfy $\alpha < 14.7^\circ$ in order to guarantee positive normal contact force during the entire periodic solution. Together with the lower bound α_{min} from (18), these two inequalities form the permissible region in the space of parameters α, κ and n. This permissible region is plotted in Figure 3.2 as slices in (κ, α)-plane for values of $n = \{4, 5, 6, 7, 8\}$. One can see that this imposes a significant limitation on the allowed parameter values. The permissible region of parameter values for maintaining contact is much smaller than the region delineated in [14] under the requirement of forward rolling only. In fact, one can see from Figure 3.2 that periodic motion of the RW which maintains contact can never exist for slope angle α steeper than 26°.

Next, we consider the bounds on contact forces which are induced by a finite coefficient of friction μ. Let the ratio of tangential to normal contact forces be denoted by $\sigma = f_t/f_n$. The friction inequality constraint (3) implies that $|\sigma(t)| \leq \mu$ must be

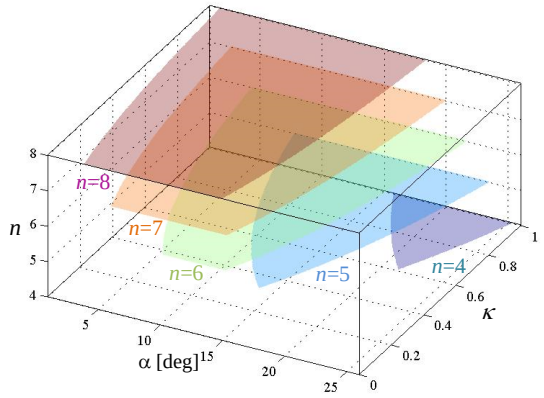

FIG. 3.2. *Regions of parameters κ, α, n for which the periodic solution exists and maintains contact with positive normal force.*

satisfied along the entire motion. Using the expression for the contact forces (19) and the energy relation (13), the ratio σ along the periodic solution with $\dot{\theta}_0{=}\dot{\theta}^*$ is a function of θ only, which is given by

$$\sigma(\theta) = \frac{\Big(3\cos(\alpha+\theta) - (\dot{\theta}^*)^2 - 2\cos(\alpha-\pi/n)\Big)\sin\theta - \kappa\sin\alpha}{\Big(3\cos(\alpha+\theta) - (\dot{\theta}^*)^2 - 2\cos(\alpha-\pi/n)\Big)\cos\theta + \kappa\cos\alpha}. \tag{22}$$

For a given value of the parameters α, κ and n, there exists a critical coefficient of friction μ_c which is the minimal value of μ required in order to satisfy the friction inequality (3) during the periodic solution. The critical value μ_c is given by

$$\mu_c = \max\{|\sigma(\theta)| : \quad \theta \in [-\pi/n, \pi/n]\}. \tag{23}$$

As an example, Figure 3.3(a) plots the force ratio $\sigma(\theta)$ along the periodic solution for parameter values of $n{=}10$, $\kappa{=}1/3$ and $\alpha{=}13^\circ$, for which the critical value is $\mu_c = 0.91$, which is attained at the endpoint $\theta{=}\pi/10$. Note that this value of μ_c is rather large, and hard to achieve in practice. Thus, it is very likely that for realistic values of friction coefficient μ, the RW dynamics will not satisfy the assumption of sticking contact. Furthermore, since $\sigma(\pi/10) < 0$, it is expected that forward slippage down the slope will evolve.

Another constraint which must be maintained in order to ensure sticking contact is concerning the contact impulse at the impact event. In particular, the ratio of tangential to normal contact impulses, defined as $\tilde{\sigma}$, must satisfy

$$|\tilde{\sigma}| = \left|\frac{\tilde{F}_t}{\tilde{F}_n}\right| \le \mu. \tag{24}$$

Using the sticking impact equation (37) and the expressions in (11), the value of $\tilde{\sigma}$ in the periodic solution is given by

$$\tilde{\sigma} = \frac{\sin(2\pi/n)}{2(\kappa + \cos^2(\pi/n))}. \tag{25}$$

This (negated) value is marked by '$\times$' at the right end of the plot in Figure 3.3(a). It can be seen that for the chosen parameter values, the periodic solution satisfies

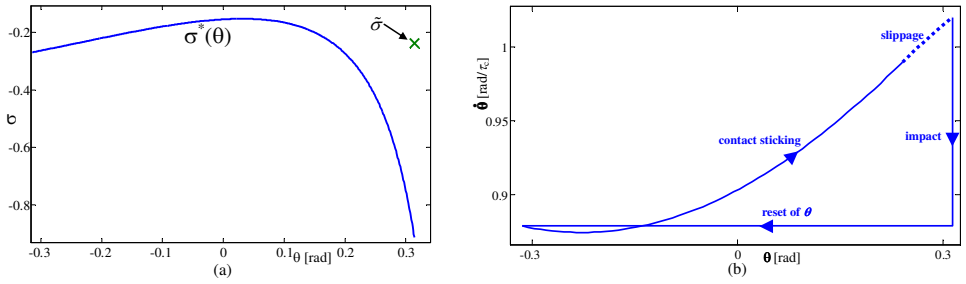

FIG. 3.3. *(a) Plot of the tangential-to-normal contact force ratio $\sigma^*(\theta)$ along the no-slip periodic solution (Type A). '$\times$' denotes the ratio $\tilde{\sigma}$ of the components of the contact impulse. (b) Trajectory in $(\theta, \dot{\theta})$-plane of Type B periodic solution with sticking impact and stick-slip transition for μ=0.4.*

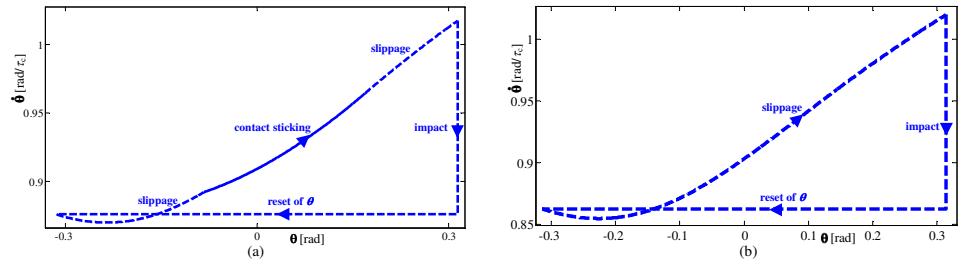

FIG. 3.4. *Trajectories of periodic solutions in $(\theta, \dot{\theta})$-plane: (a) Type C solution with slipping impact and slip-stick-slip transitions for μ=0.24. (b) Type D solution with complete slippage for μ=0.23*

$|\tilde{\sigma}| < \mu_c$, so that the impact can maintain contact sticking as long as the continuous-time motion does. When the friction coefficient μ is decreased below its critical value μ_c, contact slippage begins to evolve, as discussed next.

3.3. RW– analysis of stick-slip dynamics. When the frictional inequality (3) cannot be satisfied under sticking contact, the contact begins to slip. The detailed formulation of the rimless wheel's dynamics and impact law under slippage are given in Appendix A. In what follows, we numerically investigate the influence of changes in the coefficient of friction on hybrid periodic solutions of the RW model. In particular, we investigate transitions from sticking to slippage and vice versa, while focusing on hybrid periodic solutions and their stability.

Choosing representative parameter values as n=10, κ=1/3 and α=13°, the critical friction coefficient has already been found as μ_c=0.91. Upon varying the value of μ, four different types of periodic solutions have been found, denoted as Types A,B,C and D, which are detailed as follows. Type A solutions which exist for $\mu \geq 0.91$, involve no slippage at the contact. Type B solutions which exist for $\mu \in [0.25, 0.91]$ involve a sticking impact followed by a transition from stick to slip. Animation of this type of periodic motion can be found in the supplementary material [87]. Type C solutions which exist in the narrow range of $\mu \in (0.24, 0.25)$ involve a slipping impact followed by slip $\rightarrow$ stick $\rightarrow$ slip transitions. Finally, Type D solutions which exist for $\mu \in [0.1, 0.32]$ involve slipping impact followed by forward slippage during the entire motion. Note that in this special type of solution, $x(t)$ and $\dot{x}(t)$ are not periodic, but $\theta(t)$ and $\ddot{x}(t)$ are periodic since $\ddot{\theta}$ and $\ddot{x}$ depend on $\theta, \dot{\theta}$ and $\text{sgn}(\dot{x})$ only (see eq. (42)

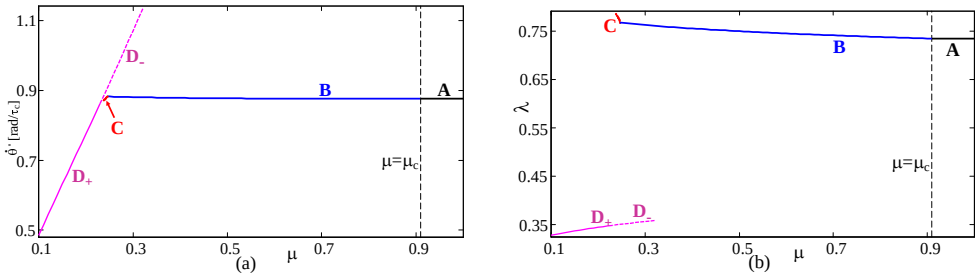

FIG. 3.5. *(a) Plot of the fixed point $\dot{\theta}^*$ of periodic solutions of the RW as a function of μ. (b) Plot of the eigenvalue λ of $D\Pi$ for the periodic solutions as a function of μ. The labels A,B,C,D correspond to the periodic solutions of Types A,B,C,D, respectively*

in Appendix A). Thus, this solution has a constant change in the slippage velocity $\dot{x}$ during each period of the solution, which is denoted by $\Delta\dot{x} = \dot{x}^+_{k+1} - \dot{x}^+_k$.

Plots of solution trajectories of Types A,B,C,D in $(\theta, \dot{\theta})$-plane for representative values of μ are shown in Figures 3.1(b),3.3(b),3.4(a),3.4(b), respectively, where motion under sticking contact appears as a solid curve while motion under slippage appears as a dashed curve. Figure 3.5(a) plots the change in the fixed point $\dot{\theta}^*$ of the Poincaré map for each type of periodic solution as a function of μ, where Type D solutions are sub-divided into Type D_+ for which $\Delta\dot{x} > 0$ and Type D_- for which $\Delta\dot{x} < 0$. Interestingly, the figure indicates that Type D_- solutions *co-exist* with Type B or Type C solutions for a given value of μ, where convergence to either of the solutions is determined by initial conditions, and particularly the slippage velocity $\dot{x}(0)$.

Figure 3.5(b) plots the change in the eigenvalue λ of the Poincaré map linearization about each periodic solution, which is obtained numerically, as a function of μ. Note that for Types A and B the Poincaré map is scalar and has a single linearization eigenvalue since the one-dimensional Poincaré section can be parametrized by $\dot{\theta}$ only. On the other hand, Type C solutions with slipping impact have a two-dimensional Poincaré section parametrized by post-impact values of $\dot{\theta}$ and $\dot{x}$. Thus, the associated Poincaré map has two eigenvalues, and the largest magnitude $\lambda_{max} = \max\{|\lambda_1|, |\lambda_2|\}$ is plotted in this branch of solutions in Figure 3.5(b).

The Poincaré section for Type D solutions is again one-dimensional and can be parametrized by $\dot{\theta}$ only since these solutions are not affected by $\dot{x}(t)$ as long as it does not reverse its sign. Thus, the Poincaré map is scalar and has a single linearization eignevalue λ which is shown on the plot in Figure 3.5(b) in solid (Type D_+) or dashed (Type D_-) lines. It can be seen that for the chosen parameter values, the low eigenvalue $\lambda \approx 0.35$ indicates rapid convergence to Type D periodic solution. However, note that these solutions can be considered as "asymptotically stable" only with respect to θ and $\dot{\theta}$, and are neutrally stable with respect to small changes in $\dot{x}$. More importantly, asymptotic convergence to Type D_- solution under initial conditions with $\dot{x}(0) > 0$ cannot actually occur, since $\Delta\dot{x} < 0$ implies that after a finite number of impacts $\dot{x}$ crosses zero and this periodic solution ceases to exist due to loss of slippage. That is, the one-dimensional Poincaré map under slippage does not account for the state variable $\dot{x}$, and thus it cannot provide a complete description of the RW dynamics.

As an example, we simulate the RW model with the same physical parameters and friction coefficient μ=0.3, under initial conditions of $\theta = -\pi/10$, $\dot{\theta} = 1.12$, and $\dot{x} = 0.7$. Figure 3.6(a) plots the solution trajectory in $(\theta, \dot{\theta})$-plane as thin lines, while

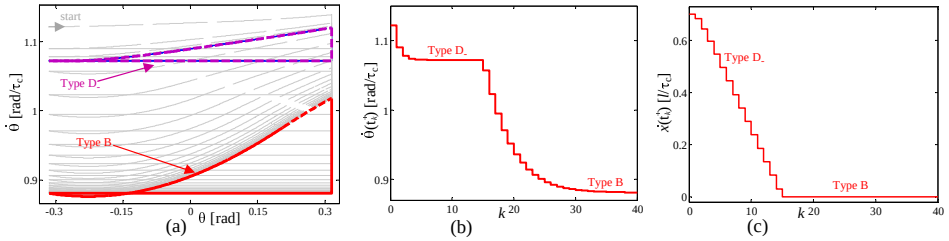

FIG. 3.6. *(a) Trajectories of solution in $(\theta, \dot{\theta})$-plane, with Type* D$_-$ *and Type B periodic solutions (thick curves); Discrete series of post-impact values of (b) $\dot{\theta}(t_k^+)$ and (c) $\dot{x}(t_k^+)$*

the loops of thick curves denote the two periodic solutions of Type B and Type D$_-$. Figures 3.6(b) and (c) plot the discrete series of post-impact values of $\dot{\theta}(t_k^+)$ and $\dot{x}(t_k^+)$, respectively. It can be seen that the motion of the RW first rapidly converges towards the Type D periodic solution with $\dot{\theta}^*$=1.072. This solution involves forward slippage with decreasing velocity of $\Delta\dot{x} = -0.0517$. Thus, after k=15 impacts, the slippage velocity $\dot{x}$ vanishes. The solution then converges to the co-existing Type B periodic solution with $\dot{\theta}^*$=0.8807, which involves sticking impact followed by stick-slip transition.

3.4. RW– regions of attraction of periodic solutions. We now analyze regions of attractions of stable periodic solutions of the rimless wheel. This subject has been extensively studied by Coleman [14], who identified three possible steady-state scenarios: (i) the stable periodic motion downhill; (ii) rocking back and forth on two spokes until coming to a rest at a two-contact position; (iii) reaching the (unstable) upright equilibrium position of the rimless wheel in infinite time. They have found the regions of attractions of scenarios (i) and (ii) in terms of initial post-impact angular velocity $\dot{\theta}_0$, and also the discrete series of $\dot{\theta}_0$ values for which scenario (iii) is reached after some finite number of impacts. It is shown in [14] that both scenarios (ii) and (iii) can never occur for steep slopes that satisfy $\alpha > \pi/n$. For shallow slopes $\alpha < \pi/n$, scenarios (ii) and (iii) can occur for negative $\dot{\theta}_0$ or for sufficiently low values of $\dot{\theta}_0 > 0$ which result in sign reversal of $\dot{\theta}$, i.e. backward rolling.

A crucial fact is that in the work [14], not only slippage was not considered, i.e unbounded friction was assumed, but also the possibility of contact detachment due to zero-crossing of the normal contact force f_n was completely ignored. From the expression for f_n in (19) and the relation (13), it can be seen that large values of $|\dot{\theta}_0|$ may cause contact detachment, and thus they must be excluded from the region of attraction. We now rederive the region of attraction of the stable periodic solution (i) of downward motion while accounting for the requirement of preserving contact $f_n > 0$. We begin with the simplifying assumption of unbounded friction $\mu \to \infty$, and then continue to the case of finite friction.

Region of attraction under unbounded friction: First, one has to require that the parameters κ, α and n are in the permissible region shown in Figure 3.2, which ensures that no contact detachment occurs along the periodic solution with $\dot{\theta}_0 = \dot{\theta}^*$. For parameter values of n=10, κ=1/3, this implies that the slope angle is bounded by $\alpha < 14.7°$. Additionally, in order for the periodic solution with $\dot{\theta}_0 = \dot{\theta}^*$ given in (16) to exist without rolling backwards, i.e. $\dot{\theta}(t) > 0$, the slope angle must satisfy $\alpha > 1.4°$, according to equation (18). For other initial conditions $\dot{\theta}_0 \neq \dot{\theta}^*$, the initial angular velocity must be sufficiently large in order to prevent backward rolling.

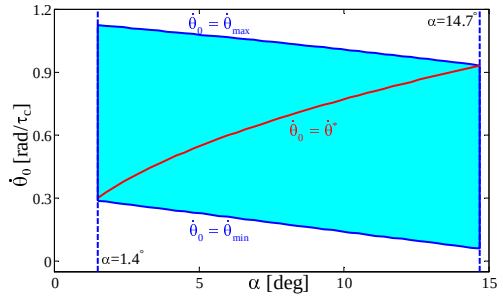

FIG. 3.7. *Region of attraction of the periodic solution in terms of* $\dot{\theta}(0)$ *as a function of* α *for unbounded friction.*

Using the energy relation (13) and requiring that $\dot{\theta} > 0$ at the upright equilibrium $\theta = -\alpha$ imposes a constraint on $\dot{\theta}_0$ as

$$\dot{\theta}_0 > \dot{\theta}_{min} = \sqrt{2(1 - \cos(\alpha - \pi/n))}. \tag{26}$$

Additionally, one has to ensure that contact is maintained, i.e. $f_n(t) > 0$. Using the expression for f_n in (19), and the energy relation (13), it can be proven (see Appendix B) that between two consecutive impacts, f_n attains its minimum value at the pre-impact state where $\theta = \pi/n$. Moreover, it can also be shown that it suffices to guarantee that the requirement $f_n(\theta = \pi/n) > 0$ is satisfied at the first impact only in order to guarantee that $f_n > 0$ during the entire solution. Using equations (13),(19) and the requirement $f_n(\theta = \pi/n) > 0$ then gives the upper bound on the initial angular velocity as $\dot{\theta}_0 < \dot{\theta}_{max}$ where

$$\dot{\theta}_{max} = \sqrt{3\cos(\alpha + \pi/n) - 2\cos(\alpha - \pi/n) + \kappa \frac{\cos(\alpha)}{\cos(\pi/n)}}.$$

Figure 3.7 plots the interval of convergent initial conditions $(\dot{\theta}_{min}, \dot{\theta}_{max})$ in a shaded region as a function of α, for n=10 and κ=1/3. The solid curve represents the initial condition of the periodic solution $\dot{\theta}_0 = \dot{\theta}^*$. It can be seen that for α=1.4°, $\dot{\theta}^*$ coincides with the lower bound $\dot{\theta}_{min}$, meaning that for initial conditions of $\dot{\theta}_0 = \dot{\theta}^*$, the RW goes to its upright position in infinite time and a periodic solution is never reached. At the other end, for α=14.7°, $\dot{\theta}^*$ coincides with the upper bound $\dot{\theta}_{max}$, meaning that the periodic solution ends with contact detachment. Thus, the interval $\dot{\theta}_0 \in (\dot{\theta}_{min}, \dot{\theta}_{max})$ is the region of attraction of the stable periodic solution of the RW which satisfies the requirement of no contact detachment under the assumption of unbounded friction. In Particular for κ=1/3 and α=13° these bounds are given by $\dot{\theta}_{min}$=0.0872 rad/τ_c and $\dot{\theta}_{max}$=0.9595 rad/τ_c. These values will be used as references for comparison with the case of finite coefficient of friction, which is studied next.

Regions of attraction under finite friction: Under a finite coefficient of friction μ, stable periodic solutions with stick-slip transitions are possible. Under perturbation in the initial post-impact angular velocity $\dot{\theta}_0$, solutions that involve slippage are allowed as long as they eventually converge to the original periodic solution, while initial conditions for which slippage ends at contact detachment are excluded. Since the slippage dynamics is not energy-preserving, the region of attraction of the periodic solutions that involve slippage can be obtained only numerically.

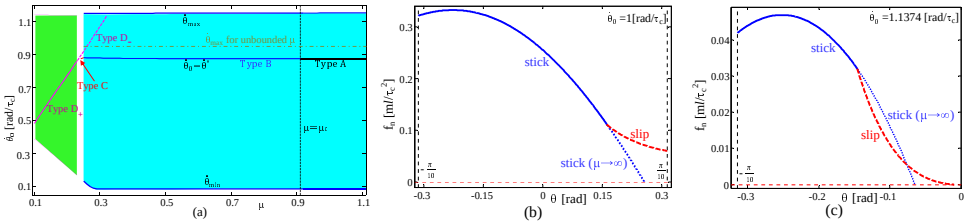

FIG. 3.8. *(a) Regions of attraction (shaded) of stable periodic solutions of Types A, B and* D_+ *in terms of initial angular velocity* $\dot{\theta}_0$ *as a function of* μ*; Normal contact force* f_n *as a function of orientation angle* θ *for* μ=1 *and (b)* $\dot{\theta}_0$=1*, (c)* $\dot{\theta}_0$=1.1374 *(solid curve- sticking, dashed curve- slippage, dotted curve- continuation of sticking for* $\mu \to \infty$*).*

We have studied periodic solutions of Types A, B and D_+, which are shown in Figure 3.8(a) for parameter values of n=10, κ=1/3 and α=13° while the friction coefficient μ is varied. Upper and lower bounds on the initial post-impact angular velocity $\dot{\theta}_0$ which result in convergence to the periodic solutions while avoiding backward rolling and contact detachment were obtained numerically. These bounds are plotted as a function of μ in Figure 3.8(a) as upper and lower curves $\theta_{min}(\mu)$ and $\theta_{max}(\mu)$ which are enclosing the initial condition of periodic solutions θ^* for Types A, B and D_+ solutions.

For Type B solutions of stick-slip with sticking impact, it can be seen that the lower bound $\dot{\theta}_{min}$ has a constant value of 0.0872 rad/τ_c for $\mu > 0.29$, which is the same value obtained for $\dot{\theta}_{min}$ in (26) for the case of unbounded friction. The reason for this is the fact that Type B solutions start with motion under sticking contact and switch to slippage only after passing the upright equilibrium, thus the condition for avoiding backward rolling is the same as the one obtained for no-slip motion. When $\mu < 0.29$, transition to slippage occurs before reaching the upright equilibrium, and thus backward rolling is affected by the slippage dynamics (eq. (42) in Appendix A), which results in different values of $\dot{\theta}_{min}$ that depend also on μ. As for the upper bound $\dot{\theta}_{max}$, it changes very slowly with μ, and tends to a constant value of approximately 1.14 rad/τ_c for large μ. Remarkably, this value is significantly larger than the value of $\dot{\theta}_{max}$=0.9595 rad/τ_c for unbounded friction, which appears as a dash-dotted line in Figure 3.8(a). The reason for this discrepancy, which persists even for very large but finite values of μ, is the observation that in a transition from contact sticking to slippage the contact forces change continuously but not smoothly. Thus, the transition to slippage changes the derivative $\dot{f}_n(t)$ to a larger value which delays the contact detachment.

As an example, Figure 3.8(b) plots the normal contact force f_n as a function of the angle θ for $\dot{\theta}_0$=1 rad/τ_c and μ=1. The solution begins with no-slip motion (solid curve) and at θ=0.163 rad it switches to slippage (dashed curve). The dotted curve is the continuation of $f_n(\theta)$ under no-slip motion with unbounded friction. It can be seen that in motion without slippage (dotted curve), f_n was supposed to reach zero (contact detachment) at θ=0.256 rad/τ_c, whereas in the actual motion under slippage f_n remains positive until impact at $\theta=\pi/10$. Thus, the initial angular velocity $\dot{\theta}_0$ can be further increased above 0.9595 rad/τ_c. The maximal allowed value of $\dot{\theta}_0$ is obtained numerically as $\dot{\theta}_{max}$=1.1374. Figure 3.8(c) plots the normal contact force $f_n(\theta)$ for the critical case of $\dot{\theta}_0=\dot{\theta}_{max}$. It can be seen that contact detachment ($f_n = 0$) occurs at an intermediate angle of $\theta = -0.01$ rather than at impact. Since avoiding contact detachment turns out to be a key consideration in the response to

initial perturbations, one can thus conclude that slippage significantly *enlarges* the region of attraction of Types A and B periodic solutions of the RW, even though the convergence rate is decreased (larger linearization eigenvalues, see Figure 3.5(b)).

The upper and lower bounds of initial angular velocities $\dot{\theta}_{min}$ and $\dot{\theta}_{max}$ for convergence to Type D_+ solution of complete slippage ($\dot{x} > 0$) are also plotted in figure 3.8(a), and enclose the region of attraction of this stable periodic solution. No region of attraction was computed for Type D_- solution, since this solution holds only for a finite number of impacts and then converges to Type B solution. Region of attraction of Type C solution was also not computed, since it involves 2 initial conditions $(\dot{\theta}_0, \dot{x}_0)$, and thus cannot be shown on the plot of Figure 3.8(a). Moreover, this type of solution exists only on a very narrow range of values of μ.

4. Passive dynamics of the compass biped. In this section, we analyze the dynamics of the passive compass biped (CB) model. The compass biped is a robotic model which consists of two rigid links ("legs") of length l, connected by a passive rotary joint ("hip"), see Figure 4.1(a). For simplicity, we assume that the two legs have identical point masses m located at a distance d from their endpoints ("feet"). Another point mass m_h is located at the hip joint. The robot walks passively on an inclined plane with slope angle α. The angle of the stance foot is θ_1 and the angle of the swing foot is θ_2, both measured with respect to the contact normal (y axis). The robot's coordinates are chosen as $\mathbf{q} = (\theta_1, \theta_2, x, y)^T$, where x, y denote the (constrained) position of the stance foot. The swing foot hits the ground when $\theta_1 = \theta_2$. Using the formulation procedure described in Section 2, the equations of motion of the robot and impulse-momentum balance can be formulated as in (2) and (4), where the explicit expressions in $\mathbf{q}, \dot{\mathbf{q}}$ are given by

$$\mathbf{M}(\mathbf{q}) = \begin{bmatrix} d^2m+l^2(m+m_h) & lm\,(l-d)\,C_{12} & [dm+l\,(m+m_h)]\,C_1 & -[dm+l\,(m+m_h)]\,S_1 \\ lm\,(l-d)\,C_{12} & m(d-l)^2 & m\,(l-d)\,C_2 & m\,(l-d)\,S_2 \\ [dm+l\,(m+m_h)]\,C_1 & m\,(l-d)\,C_2 & 2m+m_h & 0 \\ -[dm+l\,(m+m_h)]\,S_1 & m\,(l-d)\,S_2 & 0 & 2m+m_h \end{bmatrix}$$

$$\mathbf{B}(\mathbf{q}, \dot{\mathbf{q}}) = \begin{bmatrix} (d-l)lmS_{12}\dot{\theta}_2^2 \\ (d-l)mlS_{12}dot{\theta_1}^2 \\ (d-l)mS_2\dot{\theta}_2^2 - ((d+l)m+lm_h)\,S_1\dot{\theta}_1^2 \\ -lm_hC_1\dot{\theta}_1^2 - (d+l)mC_1\dot{\theta}_1^2 + (l-d)mC_2\dot{\theta}_2^2 \end{bmatrix} \quad \mathbf{W}(\mathbf{q}) = \begin{bmatrix} 0 & 0 & 1 & 0 \\ 0 & 0 & 0 & 1 \end{bmatrix}$$

$$\mathbf{G}(\mathbf{q}) = g \begin{bmatrix} -((d+l)\,m+lm_h)\sin(\theta_1+\alpha) \\ (d-l)m\sin(\alpha-\theta_2) \\ -(2m+m_h)\sin\alpha \\ (m_h+2m)\cos\alpha \end{bmatrix} \quad \tilde{\mathbf{W}}(\mathbf{q}) = \begin{bmatrix} lC_1 & lC_2 & 1 & 0 \\ -lS_1 & lS_2 & 0 & 1 \end{bmatrix} \quad \mathbf{Eu} = \begin{bmatrix} 0 \\ 0 \\ 0 \\ 0 \end{bmatrix}$$

where $S_1 = \sin\theta_1,\ S_2 = \sin\theta_2,\ S_{12} = \sin(\theta_1+\theta_2),\ C_{12} = \cos(\theta_1+\theta_2)$.

(27)

Note that after impact, the stance foot and swing foot switch roles, so that the coordinates of θ_1 and θ_2 and their velocities swapped and reversed, i.e. $\theta_1 \leftrightarrow -\theta_2,\ \dot{\theta}_1 \leftrightarrow -\dot{\theta}_2$.

4.1. Passive CB – No-slip dynamics. Assuming sticking contact, stable periodic solutions (i.e. gaits) for the passive compass biped have been demonstrated in [48] and extensively studied in [29]. As a representative example, parameter values which will be used for numerical simulations throughout this and the next section are chosen as $l = 1.6m$, $d = 0.8m$, $m = 4Kg$, $m_h = 2Kg$, $g = 9.8m/s^2$, and $\alpha = 1^\circ$. Figure 4.1(b) plots the trajectories of θ_1 and θ_2 along the periodic solution in $(\theta_i, \dot{\theta}_i)$-

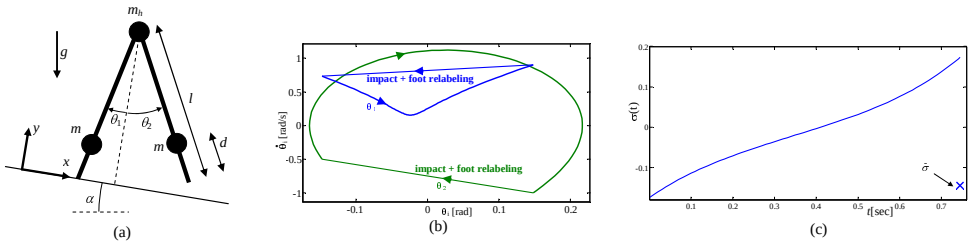

FIG. 4.1. *(a) The passive compass biped model. (b) Trajectories of a stable Gait A under sticking contact in $(\theta_i, \dot{\theta}_i)$-plane. (c) Force ratio $\sigma(t)$ along the same Gait A. '$\times$' denotes the ratio $\tilde{\sigma}$ of the components of the contact impulse.*

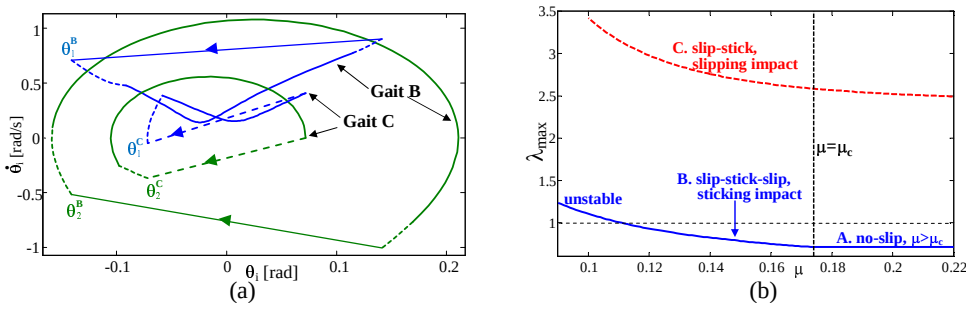

FIG. 4.2. *(a) Trajectories of two gait types for μ=0.14 in $(\theta_i, \dot{\theta}_i)$-plane: Gait B – sticking impact + slip $\rightarrow$ stick $\rightarrow$ slip, and Gait C – slipping impact + slip $\rightarrow$ stick. (b) Maximal eigenvalue λ_{max} of Gaits A,B,C as a function of μ.*

plane, where straight line segments represent the velocity jump at impact and the coordinate relabeling $\theta_1 \leftrightarrow -\theta_2$, $\dot{\theta}_1 \leftrightarrow -\dot{\theta}_2$. This type of periodic solution, which does not involve slippage, is denoted as Gait A. The Poincaré section of this solution is three-dimensional and can be parametrized by θ_1, $\dot{\theta}_1$ and $\dot{\theta}_2$, since θ_1=θ_2 at impacts. Thus, the Poincaré map linearization has three eigenvalues, whose maximal absolute value is $0.71 < 1$, which indicates that this periodic solution is locally asymptotically stable. Animation of this gait of passive walking can be found in the supplementary material [87]. Note that during a step while the swing leg passes the stance leg, there is an additional point of collision with the ground where θ_1=θ_2. This collision, which is called "scuffing", is ignored in our analysis, following the approach of [48] and [29]. Physical realizations of passive bipedal walking must provide some technical solutions for foot clearance in order to overcome this scuffing, as discussed in [48].

Next, we compute the ratio of tangential-to-normal contact forces at the stance foot. This ratio $\sigma(t)$ along the periodic solution is shown in Figure 4.1(c). The plot indicates that the minimal value of friction coefficient required to enforce contact sticking is $\mu_c = 0.175$. The ratio $\tilde{\sigma}$ of the tangential-to-normal impulse at the impact is marked as '$\times$' at the right end of the plot, and its value is given by $|\tilde{\sigma}|$=$0.145 < \mu_c$. This indicates that as long as $\mu \geq \mu_c$, the contact maintains sticking at the impact as well.

4.2. Passive CB – Stick-slip dynamics. Next, we numerically study the effect of reducing the friction coefficient μ below the critical value μ_c on existence and stability of periodic solutions with slippage. Two types of periodic gaits have been found. Gait B involves sticking impact followed by immediate transition to forward

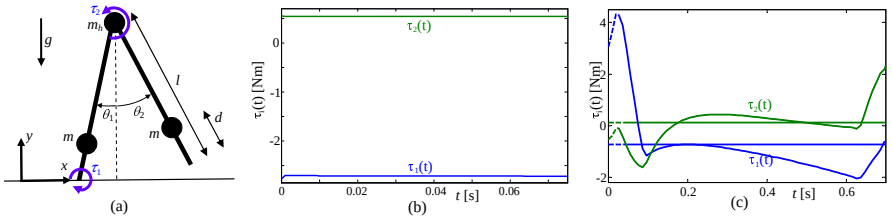

FIG. 5.1. *(a) The actuated compass biped on a horizontal plane. (b) Actuation torques $\tau_i(t)$ along the open-loop Gait I under sticking contact. (c) Actuation torques $\tau_i(t)$ along the open-loop Gait II with slipping impact. Straight horizontal lines are mean values. Dashed lines denote slippage.*

slippage and then transitions to sticking contact and to backward slippage. Gait C involves slipping impact and then a slip $\rightarrow$ stick transition. Interestingly, these two gaits are co-existing solutions under different initial conditions for the same value of μ. As an example, Figure 4.2(a) plots the trajectories of θ_1 and θ_2 along these two periodic solutions in $(\theta_i, \dot{\theta}_i)$-plane for μ=0.14, where dashed curves denote motion under contact slippage while the solid curves denote motion under sticking contact. Animation of these gaits can also be found in the supplementary material [87]. Note that the Poincaré sections of Gaits B and C differ in their dimensionality, since Gait C is characterized by the nonzero post-impact slippage velocity $\dot{x}$ in addition to $\dot{\theta}_1, \dot{\theta}_2$ and θ_1. Thus, the number of eigenvalues of the Poincaré map linearization is 3 for Gaits A and B and 4 for Gait C. Figure 4.2(b) plots the changes in the maximal eigenvalue magnitude λ_{max} for each gait type as a function of μ. It can be seen that Gait B loses stability at $\mu \approx 0.11$ where λ_{max} crosses unity, and that Gait C is unstable for all μ. Moreover, even for for $\mu > \mu_c$ where the stable no-slip Gait A exists, the unstable Gait C with slippage also co-exists for different initial conditions.

Regions of attractions of the stable Gaits A and B of the compass biped were not analyzed in this work. The reasons are the higher dimensionality of the system's state space which requires extensive numerical computation, as well as the impossibility of simple visualization of these regions which is needed in order to obtain physical intuition and insights. Finally, in our numerical simulations we did not find any periodic solution that always slips as in Type D solution of the RW model.

5. Actuated walking of the compass biped. In this section, we analyze the dynamics of the compass biped walking on a horizontal plane instead of an inclined plane as in the previous section, while gravity power is replaced by actuation torques – τ_1 at the ankle joint (i.e. the stance foot's contact point) and τ_2 at the hip joint, see Figure 5.1(a). The expressions for $\mathbf{M}(\mathbf{q}), \mathbf{B}(\mathbf{q}, \dot{\mathbf{q}}), \mathbf{G}(\mathbf{q})$, etc. in the equations of motion (2) of the actuated compass biped are identical to those of the passive model in (27), where α=0 is substituted into $\mathbf{G}(\mathbf{q})$ due to the horizontal plane. The terms of control torques in (2) are given by

$$\mathbf{E} = \begin{bmatrix} 1 & 0 & 0 & 0 \\ 1 & 1 & 0 & 0 \end{bmatrix}^T , \ \mathbf{u} = \begin{bmatrix} \tau_1 \\ \tau_2 \end{bmatrix}. \tag{28}$$

We study both open-loop and closed loop control of the joint torques, and compare between gaits with sticking and slipping impacts under open-loop and closed-loop control. In particular, we compute the energetic cost of walking, which was studied in [16]. The *specific cost* of a walking gait is the nondimensional quantity that measures

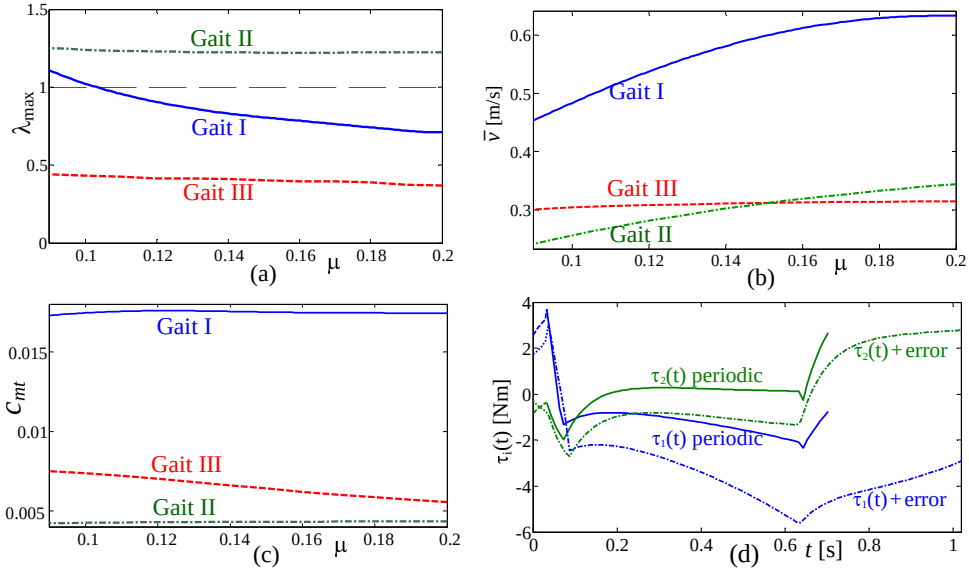

FIG. 5.2. *(a) Maximal eigenvalue λ_{max}, (b) average speed $\bar{v}$, and (c) specific cost c_{mt} as a function of μ for: open-loop Gait I with sticking impact (solid), open-loop Gait II with slipping impact (dash-dot) and feedback controlled Gait III (dashed). (d) Control torques $\tau_i(t)$ under Gait III with PD control law. Solid lines - steady-state torques along the periodic solution. Dash-dotted lines - transient torques under initial angle perturbation of 2° until first impact. Dashed lines denote slippage.*

energy expenditure per walking distance, which is defined in [16, 26] as

$$c_{mt} = \frac{W}{mgS} = \frac{1}{mgS}\int_0^T \mathbf{Eu}(t)\cdot\dot{\mathbf{q}}(t)dt, \tag{29}$$

where T is the time period of one step, W is the total mechanical work expended by the actuators during a full period, S is the distance traveled in one step, and mg is the robot's weight. For passive walking on a slope, an alternative definition for c_{mt} is proposed in [26], but it depends solely on the slope angle and not on the gait kinematics, and thus it is not considered here. On the other hand, for actuated walking c_{mt} depends also on the gait kinematics, and thus it can be used for comparing the energetic efficiency of different gaits. An additional measure used for comparing different gaits is the average speed, which is defined as $\bar{v} = S/T$.

First, two open-loop gaits with constant actuation torques are introduced, which are based on "inverse-dynamics" computed torques (cf. [52]) under prescribed gait kinematics, as follows. Choosing a given periodic trajectory of the robot $\mathbf{q}(t)$, it can be directly substituted into the dynamic equations of motion (2) in order to extract the torques $\tau_i(t)$ which are required for generation of the chosen gait. Motivated by idea from [16], the first chosen reference trajectory $\mathbf{q}(t)$ is a no-slip periodic solution of type Gait A of the passive compass biped on a slope, which is shown in Figure 4.1(b). Substituting $\mathbf{q}(t)$ and its derivatives into (2) on a horizontal plane ($\alpha = 0$), one obtains the torque profiles $\tau_1(t), \tau_2(t)$ which are plotted in 5.1(b). Since the torques are nearly constant during the entire motion, they can be approximated by constant values. Gait I is thus defined by the application of constant actuation torques $\tau_1 = -2.73$ and $\tau_2 = 0.54$, in open loop. (It is assumed that the controller is capable

of detecting which foot is currently in contact, and applies the ankle torque τ_1 at that foot). The second actuated gait is generated in a similar way, where the chosen reference trajectory is Gait C of the passive compass biped on a slope, which involves slipping impact. This gait is plotted in Figure 4.2(a). Substituting $\mathbf{q}(t)$ and its derivatives into (2) for $\alpha = 0$ and $\mu = 0.2$ results in the torque profiles $\tau_1(t), \tau_2(t)$ which are plotted in 5.1(c), where dashed lines denote slippage. Despite the larger variances of the torques, they are still approximated as constants by choosing their mean values, shown as straight horizontal lines. Gait II is thus defined by applying the constant torques $\tau_1 = -0.69$ and $\tau_2 = 0.12$ in open loop. Finally, Gait III which involves closed-loop control is generated by choosing a reference trajectory for the joint angles only, denoted by $\theta_1^r(t)$ and $\theta_2^r(t)$, which are taken from the passive Gait C with slipping impact in Figure 4.2(a). In order to track this kinematic trajectory, the actuation torques are then determined by a PD feedback law with phase resetting [4, 53] as:

$$\tau_i = -k_p(\theta_i - \theta_i^r(\phi)) - k_d(\dot{\theta}_i - \dot{\theta}_i^r(\phi)), \tag{30}$$

where $k_p, k_d > 0$ are feedback gains and ϕ is the *phase* of the gait with respect to the time of the last impact $\phi = t - t_c$. It is assumed here that the robot can detect the impact event and then immediately "reset" the time ϕ of the reference trajectory. The values of the control gains were tuned by hand as $k_p = k_d = 15$.

For each of the three gaits, the friction coefficient was varied within the range $\mu \in [0.09, 0.2]$, and periodic solutions were numerically found under the chosen control torques. Figure 5.2(a) plots the maximal linearization eigenvalue λ_{max} of each periodic solution as a function of μ. It can be seen that Gait I is stable for $\mu > 0.11$ and loses stability when μ is decreased below 0.11. Gait II with slipping impact is always unstable, whereas the feedback-controlled Gait III is strongly stable with $\lambda_{max} < 0.5$ for all μ. The average speeds $\bar{v}$ for each gait are plotted as a function of μ in Figure 5.2(b). It can be seen that Gaits II and III with slipping impact are significantly slower than Gait I with sticking impact, where the main reason is the difference in the step length S between the two gaits. (This difference can clearly be seen by comparing the angles at impact $\theta_1 = \theta_2$ of the two reference trajectories of passive Gaits B and C in Figure 4.2(a): 8° for Gait B with sticking impact and 4° for Gait C with slipping impact).

The specific cost of walking c_{mt} defined in (29) is plotted as a function of μ for each gait. Remarkably, it can be seen that Gait II with slipping impact has specific cost c_{mt} which is approximately 4-fold smaller than that of Gait I with sticking impact. The explanation for this striking difference lies in the fact that even though the friction force dissipates energy during continuous-time slippage, the energy loss due to slipping impact turns out to be significantly smaller than the loss due to sticking impact. As a particular example, under friction coefficient $\mu = 0.2 > \mu_c$, the energy loss due to sticking impact in Gait I is $0.806J$. Since there is no dissipation due to slippage during the step, this is precisely the total work of the actuators W. On the other hand, in Gait II the energy dissipation due to foot slippage during the step is $0.078J$, but the energy loss at the slipping impact is only as small as $0.022J$, so that the total work expended by the actuators is $W = 0.1$, which is 8 times smaller than that of Gait I. This ratio is mitigated by the fact that the step length of Gait II is twice shorter than that of Gait I ($0.23m$ vs. $0.47m$), so that the specific cost c_{mt} of Gait II is 3.86 smaller than that of Gait II for $\mu = 0.2$ (0.0044 vs. 0.017).

The plots in Figure 5.2 indicate that the feedback law in Gait III stabilizes the

open-loop unstable Gait II while its cost of transport c_{mt} is only slightly increased. This demonstrates that the energetic advantage of gaits with slipping impact can be exploited while stability is guaranteed via feedback. Of course, the fast convergence from initial perturbations comes at a price of large control torques in the transient phase. This is demonstrated in Figure 5.2(d), where the control torques $\tau_i(t)$ under initial perturbation in the angles as $\theta_1(0)=\theta_2(0)=\theta^* + 2^\circ$, are plotted in dash-dotted line, overlayed on the steady-state torques (solid lines). Note that under this initial error the step duration until first impact is longer than the steady-state period, and that convergence to the periodic solution is achieved after few steps (not shown in the plot). Importantly, Gait III exists under the same control law and reference trajectory for a wide range of the friction coefficient μ , including also $\mu > \mu_c$. That is, this control law is robust with respect to changes in μ, and enforces foot slippage even for large friction for which a contact-sticking gait co-exists. The main disadvantage of this gait compared to Gait I is the decrease in the average speed and step length. Several numerical attempts to improve $\bar{v}$ by changing the reference trajectory of $\theta_i^r(t)$ were successful, but resulted in significant increase in the specific cost c_{mt} due to deviation of the resulting periodic trajectory from that of the passive Gait C. This finding is in agreement with the claim in [16] that kinematic trajectories taken from passive dynamics are, in some sense, "energetically economical".

6. Concluding discussion. In this paper, we investigated simple and low dimensional models of dynamic bipedal walking under possible foot slippage. We have found stable and unstable periodic solutions with stick-slip transitions for passive walking of the rimless wheel and the compass biped models. Co-existence of solutions with sticking and slipping impact has been revealed, and the region of attraction of stable solutions has been found numerically for the rimless wheel model for both unbounded and finite friction, while accounting for the critical requirement of maintaining positive normal contact force, which was not considered in [14]. It has been found that accounting for slippage significantly enlarges the region of attraction of periodic solutions of the rimless wheel, even though the convergence rate is decreased (larger linearization eigenvalues). For the actuated compass biped on a horizontal plane, we have found periodic gaits with sticking and slipping impact based on their respective kinematic trajectories of passive dynamics, under open-loop control of constant torques. Then, we have shown that a PD control law with phase reset can stabilize the (open-loop unstable) periodic gait with slipping impact, yielding decrease in the average speed and significant improvement in the energetic efficiency. The performance of this control law is remarkably robust with respect to changes in the friction coefficient, and enforces foot slippage even for large friction. The values of the gains for the control law were chosen arbitrarily after a very short session of trial and error, without any attempt for optimization. The feedback control law presented in the paper was a very simple one and its only goal was to illustrate that the unstable open-loop gait can be easily stabilized via feedback while maintaining its energetic economy properties. Deeper analysis of tuning the control parameters or choosing more sophisticated control laws for improved performance are beyond the scope of this paper.

We now briefly discuss limitations of our results and propose possible directions for future extensions of the research. First, in our work we did not distinguish between static and dynamic friction. Incorporation of more detailed models of friction forces might yield more physically realistic results, at the price of significant complication of the hybrid system governing the system's dynamics. Second, our work only consid-

ered parameter values for which the dynamic solution was unique and consistent, and did not account for friction-related inconsistency problems associated with Painlevé's paradox [47, 59], as well as the related scenario of dynamic jamming [57] where the frictional contact force grows unbounded in finite time. Preliminary numerical checks indicate that these problems may indeed arise in passive walking of the rimless wheel and compass biped models, and detailed characterization is currently under investigation [54]. Third, it is proposed to extend the work in order to study the effect of foot slippage in detailed models of realistic legged robots with more degrees of freedom and possibly more than two legs. In such cases, the analysis and parametric study will necessarily be only numeric.

The present work only considered the dynamics and contact interaction for models which are composed of rigid bodies. However, it has been argued that in legged animal locomotion, structural elasticity has a key contribution to the dynamical behavior [37]. Inspired by this observation, two simple low-order models of biological DLL has been proposed in the literature — the spring loaded inverted pendulum (SLIP) which models humans and large mammals in sagittal plane [8], and the lateral leg spring (LLS) which models sprawled insects in horizontal plane [66]. An intriguing open problem is incorporation of stick-slip contact transitions into these two models and analyzing the influence of foot slippage on the dynamics. Preliminary steps in this challenging direction have already been made in the works [67] and [85]. Finally, in the longer term this work might also pave the way towards better understanding of rapid locomotion of large mammalian herd animals. In this regime of scale and speeds, the load of limbs becomes so large that a single high-speed misstep could lead to bone breakage and severely reduced chances of survival [22]. Recent work found large variation in the duration of the slip phase in galloping horses [72]. It is possible that horses adapt their gaits to impose slippage not only for improving energetic efficiency, but also as a mechanism for safely dissipating excess momentum, in order to maintain feasible ground forces at their limbs and avoid potential injury.

In conclusion, the influence of foot slippage on dynamic legged locomotion is far from being completely understood, but the present work showed an initial glimpse into this challenging problem, and will hopefully motivate further investigation.

Appendix A. Detailed formulation of the dynamic equations.

A.1. Continuous-time dynamic equations. The dynamic equations of motion for the system are derived as follows. Let $\mathcal{T}(\mathbf{q}, \dot{\mathbf{q}})$ be the total kinetic energy of the robot, and let $\mathcal{V}(\mathbf{q})$ be the robot's gravitational potential energy. The equations of motion are then formulated by using standard derivation of constrained Euler-Lagrange's equations (cf. [52]) which result in equation (2), where

$$\mathbf{M}(\mathbf{q}) = \frac{\partial^2 \mathcal{T}}{\partial \dot{\mathbf{q}}^2}, \quad \mathbf{B}(\mathbf{q}, \dot{\mathbf{q}}) = \left[\frac{\partial}{\partial \mathbf{q}} \left(\left(\frac{\partial \mathcal{T}}{\partial \dot{\mathbf{q}}} \right)^T \right) \right] \dot{\mathbf{q}} - \left(\frac{\partial \mathcal{T}}{\partial \mathbf{q}} \right)^T, \text{ and } \mathbf{G}(\mathbf{q}) = \left(\frac{\partial \mathcal{V}}{\partial \mathbf{q}} \right)^T.$$

Under sticking contact, the constraint $\mathbf{W}(\mathbf{q}) = 0$ has to be satisfied along with equation (2). In order to compute the contact force $\mathbf{f}$ one has to differentiate this constraint with respect to time, which yields $\mathbf{W}\ddot{\mathbf{q}} + \dot{\mathbf{W}}\dot{\mathbf{q}} = 0$. Substituting the expression for $\ddot{\mathbf{q}}$ from (2) then gives the contact force under sticking contact, which is given by

$$\mathbf{f}_{stick}(\mathbf{q}, \dot{\mathbf{q}}, \mathbf{u}) = \left(\mathbf{W}\mathbf{M}^{-1}\mathbf{W}^T \right)^{-1} \left(\mathbf{W}\mathbf{M}^{-1}(\mathbf{B} + \mathbf{G} - \mathbf{E}\mathbf{u}) - \dot{\mathbf{W}}\dot{\mathbf{q}} \right), \qquad (31)$$

where the dependence in $\mathbf{q}$ and $\dot{\mathbf{q}}$ in the right hand side of (31) is suppressed for brevity.

When the expression in (31) does not satisfy the inequality (3) of Coulomb's friction law, the contact begins to slip, i.e. $v_t \neq 0$, and the contact force satisfies $f_t = -\text{sgn}(v_t)\mu f_n$. This can also be written in matrix form as

$$\mathbf{f} = \mathbf{\Gamma} f_n, \text{ where } \mathbf{\Gamma} = \begin{pmatrix} -\text{sgn}(v_t)\mu \\ 1 \end{pmatrix}. \tag{32}$$

The contact force $\mathbf{f}$ under slippage cannot be computed as in (31), since the constraint $\mathbf{W}(\mathbf{q}) = 0$ is not satisfied. Instead, one has to differentiate the single constraint on normal velocity $\mathbf{w}_n(\mathbf{q})^T\dot{\mathbf{q}} = 0$ with respect to time and substitute the expression for $\ddot{\mathbf{q}}$ from (2) in order to obtain the force as

$$\mathbf{f}_{slip}(\mathbf{q}, \dot{\mathbf{q}}, \mathbf{u}) = \mathbf{\Gamma}\left(\mathbf{w}_n^T\mathbf{M}^{-1}\mathbf{W}^T\mathbf{\Gamma}\right)^{-1}\left(\mathbf{w}_n^T\mathbf{M}^{-1}(\mathbf{B} + \mathbf{G} - \mathbf{E}\mathbf{u}) - \dot{\mathbf{w}}_n\dot{\mathbf{q}}\right). \tag{33}$$

Contact slippage is maintained as long as $v_t = \mathbf{w}_t(\mathbf{q})\dot{\mathbf{q}} \neq 0$. When v_t vanishes, a transition to sticking contact occurs if the contact force $\mathbf{f}$ in (31) satisfies (3). Otherwise, slip reversal occurs and v_t reverses its sign.

Using the state vector $\mathbf{x} = (\mathbf{x}_1, \mathbf{x}_2) = (\mathbf{q}, \dot{\mathbf{q}}) \in \mathbb{R}^{2N}$, the state equation of the system is given by

$$\dot{\mathbf{x}} = \mathcal{F}(\mathbf{x}, \mathbf{u}) = \begin{pmatrix} \mathbf{x}_2 \\ \mathbf{M}^{-1}(\mathbf{B} + \mathbf{G} - \mathbf{E}\mathbf{u} + \mathbf{W}^T\mathbf{f}) \end{pmatrix}, \tag{34}$$

where the contact force $\mathbf{f}$ in (34) is conditionally determined by (31), (3) and (33), as

$$\mathbf{f}(\mathbf{q}, \dot{\mathbf{q}}, \mathbf{u}) = \begin{cases} \mathbf{f}_{stick}(\mathbf{q}, \dot{\mathbf{q}}, \mathbf{u}) & \mathbf{w}_t(\mathbf{q}) \cdot \dot{\mathbf{q}} = 0 \text{ and } |f_t| \leq \mu f_n \\ \mathbf{f}_{slip}(\mathbf{q}, \dot{\mathbf{q}}, \mathbf{u}) & \text{otherwise} \end{cases} \tag{35}$$

Therefore, the vector field $\mathcal{F}(\mathbf{x}, \mathbf{u})$ in (34) is piecewise-continuous.

A.2. Impact law. Explicit formulation of the impact law is obtained as follows. Let $\tilde{\mathbf{v}} = \dot{\tilde{\mathbf{r}}}$ denote the velocity of the swing foot, where its tangential and normal components $\tilde{v}_t$, $\tilde{v}_n$ depend on $\mathbf{q}$ and $\dot{\mathbf{q}}$ according to

$$\tilde{\mathbf{v}} = \begin{pmatrix} \tilde{v}_t \\ \tilde{v}_n \end{pmatrix} = \begin{pmatrix} \tilde{\mathbf{w}}_t(\mathbf{q})^T \\ \tilde{\mathbf{w}}_n(\mathbf{q})^T \end{pmatrix}\dot{\mathbf{q}} = \tilde{\mathbf{W}}(\mathbf{q})\dot{\mathbf{q}}, \text{ where } \tilde{\mathbf{W}}(\mathbf{q}) = \frac{d\tilde{\mathbf{r}}}{d\mathbf{q}}. \tag{36}$$

Substituting relations (4) and (36) into the constraint $\tilde{\mathbf{v}}(t_c^+) = 0$ which stems from assuming a perfectly plastic collision, the contact impulse $\tilde{\mathbf{F}}$ can be obtained as

$$\tilde{\mathbf{F}}_{stick} = -\left(\tilde{\mathbf{W}}_c\mathbf{M}_c^{-1}\tilde{\mathbf{W}}_c^T\right)^{-1}\tilde{\mathbf{W}}_c\dot{\mathbf{q}}_c^-. \tag{37}$$

Substituting (37) into (4) then gives a linear relation between the pre-impact and post-impact velocities as

$$\dot{\mathbf{q}}_c^+ = \left(\mathbf{I} - \mathbf{M}_c^{-1}\tilde{\mathbf{W}}_c^T(\tilde{\mathbf{W}}_c\mathbf{M}_c^{-1}\tilde{\mathbf{W}}_c^T)^{-1}\tilde{\mathbf{W}}_c\right)\dot{\mathbf{q}}_c^- = \boldsymbol{\beta}_{stick}(\mathbf{q}_c)\dot{\mathbf{q}}_c^- \tag{38}$$

where $\mathbf{I}$ is the $N \times N$ identity matrix. The impact law in (38) can be maintained only if the impulse $\tilde{\mathbf{F}}$ satisfies the frictional inequality (5). When (5) is not satisfied, slippage must occur, so that $\tilde{v}_t(t_c^+) \neq 0$. In that case, it is assumed that the tangential

impulse attains its maximal allowed magnitude $\tilde{F}_t = s\mu\tilde{F}_n$, where $s = -\text{sgn}(\tilde{v}_t(t_c^-))$. In order to compute the normal impulse $\tilde{F}_n$, one has to substitute the no-rebound requirement $\tilde{v}_n(t_c^+) = 0$ into (4) in order to obtain the contact impulse $\tilde{\mathbf{F}}$ at slipping impact, which is given by

$$\tilde{\mathbf{F}}_{slip} = \tilde{\mathbf{\Gamma}}\tilde{F}_n = -\tilde{\mathbf{\Gamma}}\left(\tilde{\mathbf{w}}_n(\mathbf{q}_c)^T\mathbf{M}_c^{-1}\tilde{\mathbf{W}}_c^T\tilde{\mathbf{\Gamma}}\right)^{-1}\tilde{\mathbf{w}}_n(\mathbf{q}_c)^T\dot{\mathbf{q}}_c^-, \text{ where } \tilde{\mathbf{\Gamma}} = \begin{pmatrix} 1 \\ s\mu \end{pmatrix}. \quad (39)$$

Substituting (39) into (4) then gives a linear relation between the pre-impact and post-impact velocities as

$$\dot{\mathbf{q}}_c^+ = \left(\mathbf{I} - \mathbf{M}_c^{-1}\tilde{\mathbf{W}}_c^T\tilde{\mathbf{\Gamma}}\left(\tilde{\mathbf{w}}_n(\mathbf{q}_c)^T\mathbf{M}_c^{-1}\tilde{\mathbf{W}}_c^T\tilde{\mathbf{\Gamma}}\right)^{-1}\tilde{\mathbf{w}}_n(\mathbf{q}_c)^T\right)\dot{\mathbf{q}}_c^- = \boldsymbol{\beta}_{slip}(\mathbf{q}_c)\dot{\mathbf{q}}_c^-. \quad (40)$$

The laws of sticking impact (38) and slipping impact (40) can be now combined into a single impact law as $\dot{\mathbf{q}}^+ = \boldsymbol{\beta}(\mathbf{q}_c)\dot{\mathbf{q}}^-$, where $\boldsymbol{\beta}(\mathbf{q}_c)$ is conditionally defined as $\boldsymbol{\beta}_{stick}(\mathbf{q}_c)$ if inequality (5) is satisfied, and as $\boldsymbol{\beta}_{slip}(\mathbf{q}_c)$ otherwise. This impact law is equivalent to Chatterjee's algebraic impact law given in [12] under zero restitution in both normal and tangential directions (i.e. $e = e_t = 0$ in the terminology of [12]). This impact law accounts for friction limitations and thus may result in post-impact slippage, but it cannot predict slip reversal, unlike Routh's method [81]. Additional impact laws can be found in [10, 61, 76]. Note that all impact laws in the literature on legged robots, including the one considered here, assume that impulsive force acts only at the colliding foot and not on the foot that is already in contact. Generalized impact laws that involve multiple contacts can be found in [10, 61].

A.3. Dynamics of the rimless wheel under slippage. For the rimless wheel with coordinates $\mathbf{q} = (x, y, \theta)$, the kinetic and potential energies are given by

$$\begin{aligned} \mathcal{T}(\mathbf{q}, \dot{\mathbf{q}}) &= \tfrac{1}{2}m(\dot{x}^2 + \dot{y}^2 + 2\dot{x}\dot{\theta}l\cos\theta + 2\dot{y}\dot{\theta}l\sin\theta) + \tfrac{1}{2}(I_c + ml^2)\dot{\theta}^2 \\ \mathcal{V}(\mathbf{q}) &= mg(y\cos\alpha - x\sin\alpha + l\cos(\alpha+\theta)). \end{aligned} \quad (41)$$

The equations of motion can then be derived in the form (2), where all the expressions are given in (11). The equations of motion under sticking contact are detailed in part 3.2. The equations of motion under contact slippage are given below. Since the constraint $\dot{x}$=0 no longer holds during slippage, the contact force is determined by (33). Substituting the expressions in (11) into the equation of motion (2) and the expressions for the contact force in (33), one obtains the equations of motion as

$$\begin{aligned} \ddot{\theta} &= \frac{\text{sgn}(\dot{x})\,\mu f_n\cos\theta + m\sin\theta\left(g\cos\alpha - l\dot{\theta}^2\cos\theta\right)}{ml\left(\sin^2\theta + \kappa\right)} \\ \ddot{x} &= \frac{lm\sin\theta\,(1+\kappa)\,\dot{\theta}^2 - \text{sgn}(\dot{x})\,\mu f_n\,(1+\kappa) + gm\,(\kappa\sin\alpha - \cos(\alpha+\theta)\sin\theta)}{m\left(\sin^2\theta + \kappa\right)} \\ f_n &= \frac{\kappa m\left(g\cos\alpha - l\cos\theta\cdot\dot{\theta}^2\right)}{\sin\theta(\text{sgn}(\dot{x})\mu\cos\theta + \sin\theta) + \kappa} \end{aligned} \quad (42)$$

When the slippage velocity $\dot{x}(t)$ vanishes, the dynamics switches back to the contact sticking dynamics (12), as long as the contact force satisfies $|\sigma(\theta, \dot{\theta})| \leq \mu$. When the latter inequality is violated, the solution switches back to the slippage dynamics (42). The process described above is known as *stick-slip transitions*.

Since impact may occur with nonzero slippage velocity $\dot{x}^- \neq 0$, the impact law in (14) must be extended to account for the influence of $\dot{x}^-$. Assuming sticking contact at the post-impact state, the impact law is obtained from (38) and (11) as

$$\begin{pmatrix} \dot{x}^+ \\ \dot{\theta}^+ \end{pmatrix} = \begin{pmatrix} 0 & 0 \\ \frac{\cos\phi}{l(1+\kappa)} & \beta \end{pmatrix} \begin{pmatrix} \dot{x}^- \\ \dot{\theta}^- \end{pmatrix} \text{ where } \phi = \pi/n. \tag{43}$$

This sticking impact law, which reduces to (14) for $\dot{x}^-=0$, holds as long as the contact impulse satisfies the friction constraint (5). For the RW model, this inequality is given by

$$\frac{|(\kappa + \sin^2\phi)\dot{x}^- + (\sin\phi \sin 2\phi) l\dot{\theta}^-|}{\sin\phi \left(\cos\phi \dot{x}^- + (\kappa + \cos^2\phi) l\dot{\theta}^-\right)} \leq \mu \tag{44}$$

When inequality (44) is not satisfied, slipping impact occurs. Using (11) and (40), the slipping impact law is given by

$$\begin{pmatrix} \dot{x}^+ \\ \dot{\theta}^+ \end{pmatrix} = \begin{pmatrix} 1 & \frac{2l \sin 2\phi(s\mu\cos\phi - \sin\phi) + 2s\mu\kappa\sin\phi}{\cos 2\phi + s\mu \sin 2\phi - 1 - 2\kappa} \\ 0 & -\frac{4\kappa}{\cos 2\phi + s\mu \sin 2\phi - 1 - 2\kappa} - 1 \end{pmatrix} \begin{pmatrix} \dot{x}^- \\ \dot{\theta}^- \end{pmatrix}. \tag{45}$$

Appendix B. Proof of zero normal force in the RW model. According to equations (19) and (13), the normal force f_n along a solution of the RW with initial conditions $\theta(0) = -\frac{\pi}{n}$ and $\dot{\theta}(0) = \dot{\theta}_0$ is

$$f_n(\theta) = \frac{mg}{1+\kappa} \left(\left(3\cos(\alpha + \theta) - \dot{\theta}_0^2 - 2\cos(\alpha - \tfrac{\pi}{n}) \right) \cos\theta + \kappa \cos\alpha \right) \tag{46}$$

where $\alpha \in \left(0, \frac{\pi}{2}\right)$, $\kappa \in [0,1]$, $n \in \{4,5,6,...\}$, and θ varies within the interval $I_n = [-\frac{\pi}{n}, \frac{\pi}{n}]$. Normalizing the force units so that $mg = 3(1+\kappa)$, one obtains

$$f_n = \left((\cos(\alpha+\theta) - c)\cos\theta + \frac{\kappa}{3}\cos\alpha \right) = \frac{1}{2}\cos(\alpha + 2\theta) - c\cos\theta + b, \quad b, c > 0 \tag{47}$$

where $c = \frac{1}{3}(\dot{\theta}_0^2 + 2\cos(\alpha - \frac{\pi}{n})) > 0$ and $b = \left(\frac{1}{2} + \frac{\kappa}{3}\right)\cos\alpha$. One can see that f_n decreases monotonically upon increasing $\dot{\theta}_0$. We assume that along the periodic solution $\dot{\theta}_0 = \dot{\theta}^*$ the normal force is non-negative, i.e. $f_n(\theta) \geq 0$ for all $\theta \in I_n$. Our goal is to prove that if the minimum of $f_n(\theta)$ within I_n is zero, then it must be attained at the upper endpoint $\theta = \frac{\pi}{n}$. We present two proofs, where each proof holds under different assumptions on the parameters.

B.1. Proof 1. First, we assume that there exist sufficiently small value of $c = c^* > 0$ for which $f_n(\theta) > 0$ for all $\theta \in I_n$. (Otherwise, no periodic solution of the RW exists that maintains contact). Thus, let $c_{min} > c^*$ denote the minimal value of c for which $f_n(\theta) = 0$ for some $\theta \in I_n$. Therefore, any $c \leq c_{min}$ satisfies

$$c\cos\theta \leq \frac{1}{2}\cos\alpha + \frac{1}{2}\cos(\alpha + 2\theta) + b \quad \text{for all } \theta \in I_n. \tag{48}$$

We restrict the parameters α, κ and n by assuming that they satisfy the following inequality, which is crucial for this proof:

$$-9\cos(\alpha + 2\pi/n) + (3 + 2\kappa)\cos\alpha < 0. \tag{49}$$

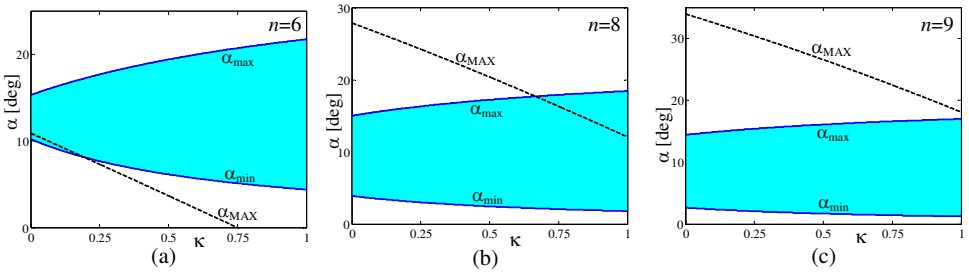

FIG. B.1. *The region $\alpha_{min} < \alpha < \alpha_{max}$ and the bound $\alpha < \alpha_{MAX}$ for (a) $n = 6$, (b) $n = 8$ and (c) $n = 9$.*

We will show later how this assumption affects the generality of the proof. The first and second derivatives of $f_n(\theta)$ are given by:

$$f_n'(\theta) = -\sin(\alpha + 2\theta) + c\sin\theta. \tag{50}$$

$$f_n''(\theta) = -2\cos(\alpha + 2\theta) + c\cos\theta. \tag{51}$$

Using inequality (48) then implies that any $c \leq c_{min}$ satisfies

$$f_n''(\theta) \leq -\frac{3}{2}\cos(\alpha + 2\theta) + b = -\frac{3}{2}\cos(\alpha + 2\theta) + \left(\frac{1}{2} + \frac{\kappa}{3}\right)\cos\alpha = w(\theta) \tag{52}$$

for all $\theta \in I_n$. Note that the function $w(\theta)$ in (52) attains its maximum within I_n at the endpoint $\theta{=}\frac{\pi}{n}$. Using (52), the bound (49) then implies that for $c = c_{min}$ one obtains $f_n''(\theta) \leq w(\frac{\pi}{n}) < 0$ for all $\theta \in I_n$. In that case, even if a critical point of $f_n(\theta)$ exists within I_n, it must be a maximum point, hence $f_n(\theta)$ attains its minimum value only at an endpoint of I_n. Finally, substitution of the values of f_n at the endpoints yields

$$f_n(-\frac{\pi}{n}) - f_n(\frac{\pi}{n}) = \frac{1}{2}\cos\left(\alpha - \frac{\pi}{n}\right) - \frac{1}{2}\cos\left(\alpha + \frac{\pi}{n}\right) > 0. \tag{53}$$

This implies that the minimum of $f_n(\theta)$ within I_n is attained at the upper endpoint $\theta{=}\frac{\pi}{n}$, which completes the proof.

Next, we study the range of parameters for which this proof is valid. For given values of κ and n, the assumption (49) implies an upper bound $\alpha < \alpha_{MAX}$. On the other hand, inequalities (34) and (37) from the paper give upper and lower bounds α_{min} and α_{max} for which the periodic solution is valid. The lower bound $\alpha > \alpha_{min}$ must be satisfied in order to ensure existence of the periodic solution with $\dot{\theta}_0 = \dot{\theta}^*$, while the upper bound $\alpha < \alpha_{min}$ must be satisfied in order to ensure positive contact force $f_n(\theta = \frac{\pi}{n}) > 0$. Figures B.1(a,b,c) plot the region $\alpha_{min} < \alpha < \alpha_{max}$ (shaded) and the upper bound $\alpha = \alpha_{MAX}$ (dashed line) as a function of κ for $n = 6, 8, 9$ respectively. It can be seen that for $n \geq 9$, the assumption (49) holds for the entire region $\alpha_{min} < \alpha < \alpha_{max}$. For $n = 6, 7, 8$ the assumption (49) holds only for part of this region, while for $n = 4, 5$ the assumption (49) is not satisfied at all. Thus, we conclude that this proof holds for $n \geq 9$ and arbitrary κ, α.

B.2. Proof 2. The second proof takes a slightly different approach, and uses an assumption on the parameters which is less restrictive than (49). First, we define $c_0 = c_0(\alpha, \kappa, n)$ as

$$c_0(\alpha, \kappa, n) = \frac{\cos(\alpha + \frac{2\pi}{n}) + 2b}{2\cos(\frac{\pi}{n})} > 0. \tag{54}$$

This definition implies that for $c{=}c_0$, one obtains $f_n(\theta{=}\frac{\pi}{n}) = 0$. Setting $c{=}c_0$, We now need to prove that the minimum of $f_n(\theta)$ within I_n is attained at the endpoint $(\theta{=}\frac{\pi}{n})$. Instead of using assumption (49), we assume that the parameters α, κ and n satisfy the inequality

$$-2\cos(\alpha - \frac{2\pi}{n}) + \cos(\frac{\pi}{n})c_0(\alpha, \kappa, n) < 0. \tag{55}$$

We will show later that this assumption, which is necessary for the proof, has a minor effect on the generality of the result. We now focus on the interval of nonnegative angles $\theta \in I_+ = [0, \frac{\pi}{n}]$. Define the series of functions

$$g_k(\theta) = -4^k \sin(\alpha + 2\theta) + c_0 \sin\theta \tag{56}$$

for $k = 0, 1, 2, ...$ It can be verified that the series $g_k(\theta)$ satisfies $g_{k+1}(\theta) = -g_k''(\theta)$. Furthermore, $g_k(\theta)$ are related to the odd-order derivatives of the normal force $f_n(\theta)$ as

$$\frac{d^{2k+1}}{d\theta^{2k+1}} f_n(\theta) = (-1)^k g_k(\theta). \tag{57}$$

In particular, for $k{=}0$ one obtains $g_0(\theta) = f_n'(\theta)$. It can be proven (details omitted) that $g_0(\theta{=}\frac{\pi}{n}) < 0$. Note that this also implies that $g_k(\theta{=}\frac{\pi}{n}) < 0$ for all k. Additionally, it is easy to see that $g_k(0) < 0$ for all k. Moreover, there exists a sufficiently large k^* which satisfies $g_{k^*}(\theta) < 0$ for all $k > k^*$ and $\theta \in I_+$. This value of k^* is given by

$$k^* > \log_4 \left(\max \left\{ \frac{c_0 \sin\theta}{\sin(\alpha + 2\theta)},\ \theta \in I_+ \right\} \right). \tag{58}$$

Next, we prove that $g_k(\theta) < 0$ for all $\theta \in I_+$ and for all k, by backward induction in k starting from $k{=}k^*$. Suppose that $g_k(\theta)$ for some k is indeed negative for all $\theta \in I_+$. This implies that $g_{k-1}''(\theta) > 0$ for all $\theta \in I_+$. Thus, if $g_{k-1}(\theta)$ has a critical point within $\theta \in I_+$, it must be a minimum point. Therefore, the maximal value of $g_{k-1}(\theta)$ can only be attained at one of the endpoints of I_+. Since $g_{k-1}(0) < 0$ and $g_{k-1}(\frac{\pi}{n}) < 0$, we conclude that $g_{k-1}(\theta) < 0$ for all $\theta \in I_+$. Carrying this induction down to $k{=}0$, the relation (57) then implies that $f_n'(\theta) < 0$ for all $\theta \in I_+$, hence $f_n(\theta)$ has no critical point within $\theta \in I_+$.

Next, we focus on the interval of negative angles $\theta \in I_- = [-\frac{\pi}{n}, 0]$. For $k = 0, 1, 2, ...$, define the series of functions

$$h_k(\theta) = -2 \cdot 4^k \cos(\alpha + 2\theta) + c_0 \cos\theta. \tag{59}$$

It can be verified that the series $h_k(\theta)$ satisfies $h_{k+1}(\theta) = -h_k''(\theta)$. Furthermore, $h_k(\theta)$ are related to the even-order derivatives of the normal force $f_n(\theta)$ as

$$\frac{d^{2k+2}}{d\theta^{2k+2}} f_n(\theta) = (-1)^k h_k(\theta). \tag{60}$$

In particular, for $k = 0$ one obtains $h_0(\theta) = f_n''(\theta)$. It can be proven (details omitted) that $h_0(0) < 0$. Moreover, inequality (55) implies that $h_0(-\frac{\pi}{n}) < 0$. Note that this also implies that $h_k(-\frac{\pi}{n}) < 0$ and $h_k(0) < 0$ for all k, since $h_k(\theta) < h_0(\theta)$ for all $k > 0$ and all $\theta \in I_-$. Moreover, there exists a sufficiently large k^* which satisfies $h_{k^*}(\theta) < 0$ for all $k > k^*$ and $\theta \in I_-$. This value of k^* is given by

$$k^* > \log_4 \left(\max \left\{ \frac{c_0 \cos\theta}{2\cos(\alpha + 2\theta)},\ \theta \in I_- \right\} \right). \tag{61}$$

Next, we prove that $h_k(\theta) < 0$ for all $\theta \in I_-$ and for all k, by backward induction in k starting from $k{=}k^*$. Suppose that $h_k(\theta)$ for some k is indeed negative for all $\theta \in I_-$. This implies that $h_{k-1}''(\theta) > 0$ for all $\theta \in I_-$. Thus, if $h_{k-1}(\theta)$ has a critical point within $\theta \in I_-$, it must be a minimum point. Therefore, the maximal value of $h_{k-1}(\theta)$ is attained at the endpoints of I_-. Since $h_{k-1}(0) < 0$ and $h_{k-1}(\frac{\pi}{n}) < 0$, we conclude that $h_{k-1}(\theta) < 0$ for all $\theta \in I_-$. Carrying this induction down to $k = 0$, the relation (60) implies that $f_n''(\theta) < 0$ for all $\theta \in I_-$. Therefore, if $f_n(\theta)$ has a critical point within I_-, it must be a maximum point.

Finally, since $f_n(\theta)$ has no minimum point within I_- and no critical point within I_+, one concludes that its minimum within I_n is attained only at the endpoints $\theta = \pm\frac{\pi}{n}$. Using (53) , it can be shown that the minimum is attained at the upper endpoint $\theta{=}\frac{\pi}{n}$, which completes the proof.

We now study the range of parameters for which this proof is valid. For given values of κ and n, the assumption (55) implies a lower bound $\alpha > \alpha_{MIN}$. On the other hand, inequalities (34) and (37) from the paper impose upper and lower bounds $\alpha_{min} < \alpha < \alpha_{max}$ for which the periodic solution is valid. Figures B.2(a,b,c) plot the region $\alpha_{min} < \alpha < \alpha_{max}$ (shaded) and the lower bound $\alpha = \alpha_{MIN}$ (dashed line) as a function of κ for $n = 4, 5, 6$ respectively. It can be seen that for $n \geq 6$, the assumption (55) holds for the entire region $\alpha_{min} < \alpha < \alpha_{max}$. For $n = 4, 5$ the assumption (55) holds almost everywhere, except for a very small part of this region. Furthermore, numerical checks show that even in these small regions where (55) is not satisfied, the statement is still true and $f_n(\theta)$ attains its minimum at the upper endpoint of I_n and has a maximum point within I_- despite the fact that $f_n''(-\frac{\pi}{n}) > 0$, since $f_n'' < 0$ at the critical point where $f_n' = 0$. As an example, Figure B.2(d,e,f) plots $f_n(\theta), f_n'(\theta)$ and$f_n''(\theta)$, respectively, for $c = c_0$ and parameter values of $n = 4$, $\kappa = 1$ and $\alpha = 16^\circ$, for which (55) is not satisfied.

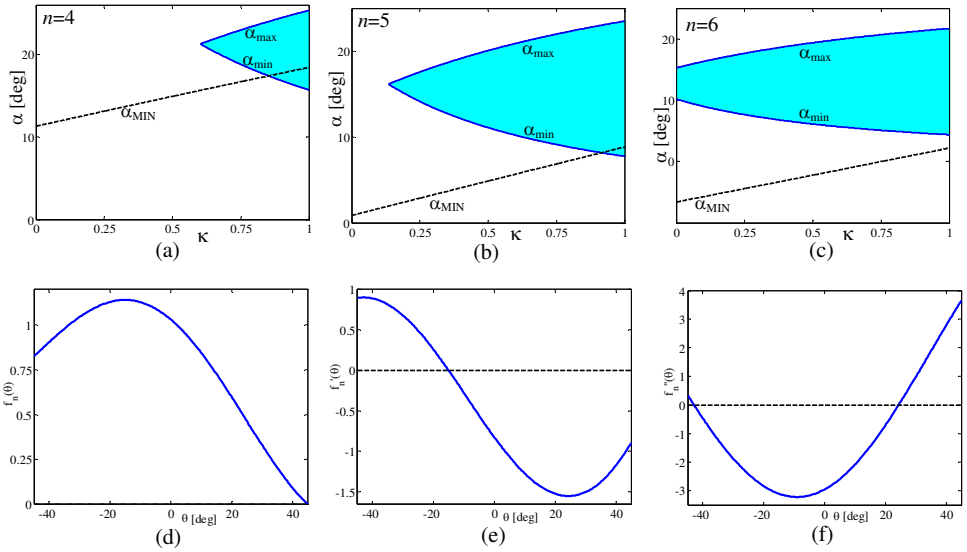

FIG. B.2. *The region $\alpha_{min} < \alpha < \alpha_{max}$ and the bound $\alpha > \alpha_{MIN}$ for (a) $n = 6$, (b) $n = 8$ and (c) $n = 9$; Plots of (d) $f_n(\theta)$, (e) $f'_n(\theta)$ and (f) $f''_n(\theta)$, for $c = c_0$, $n = 4$, $\kappa = 1$ and $\alpha = 16°$.*

REFERENCES

[1] G. AGUIRRE-OLLINGER, J. E. COLGATE, M. A. PESHKIN, AND A. GOSWAMI, *Inertia compensation control of a one-degree-of-freedom exoskeleton for lower-limb assistance: Initial experiments*, IEEE Trans. Neural Systems and Rehabilitation Engineering, 20 (2012), pp. 68–77.

[2] A. D. AMES, E. A. COUSINEAU, AND M. J. POWELL, *Dynamically stable robotic walking with NAO via human-inspired hybrid zero dynamics*, in Proceedings of the 15th ACM international conference on Hybrid Systems: Computation and Control, 2012, pp. 135–144.

[3] M. ANITESCU AND F. A. POTRA, *Formulating dynamic multi-rigid-body contact problems with friction as solvable linear complementarity problems*, Nonlinear Dynamics, 14 (1997), pp. 231–247.

[4] S. AOI AND K. TSUCHIYA, *Stability analysis of a simple walking model driven by an oscillator with a phase reset using sensory feedback*, IEEE Transactions on Robotics, 22 (2006), pp. 391–397.

[5] A. BACK, J. GUCKENHEIMER, AND M. MYERS, *A dynamical simulation facility for hybrid systems*, Lecture Notes in Computer Science, 736 (1993), pp. 255–267.

[6] M. D. BERKEMEIER AND R. S. FEARING, *Sliding and hopping gaits for the underactuated acrobot*, IEEE Trans. Robotics and Automation, 14 (1998), pp. 629–634.

[7] P. BIRKMEYER AND K. PETERSON, *DASH: a dynamic 16g hexapedal robot*, in IEEE/RSJ Conf. on Intelligent Robots and Systems (IROS), 2009, pp. 2683–2689.

[8] R. BLICKHAN AND R. J. FULL, *Similarity in multilegged locomotion - bouncing like a monopode*, Journal of Comparative Physiology A, 173 (1993), pp. 509–517.

[9] H. F. BOHN AND W. FEDERLE, *Insect aquaplaning: Nepenthes pitcher plants capture prey with the peristome, a fully wettable water-lubricated anisotropic surface*, Proc. National Academy of Sciences, 101 (2004), pp. 14138–14143.

[10] B. BROGLIATO, *Nonsmooth Mechanics*, Springer-Verlag, 1999.

[11] T. H. CHANG AND Y. HURMUZLU, *Sliding control without reaching phase and its application to bipedal locomotion*, ASME Journal on Dynamic Systems, Measurement, and Control, 105 (1994), pp. 447–455.

[12] A. CHATTERJEE AND A. RUINA, *A new algebraic rigid body collision law based on impulse space considerations*, ASME Journal of Applied Mechanics, 65 (1998), pp. 939–951.

[13] A. J. CLARK AND T. E. HIGHAM, *Slipping, sliding and stability: locomotor strategies for overcoming low-friction surfaces*, Journal of Experimental Biology, 214 (2011), pp. 1369–1378.

[14] M. J. COLEMAN, *Dynamics and stability of a rimless spoked wheel: a simple 2D system with impacts*, Dynamical Systems: an International Journal, 25 (2010), pp. 215–238.

[15] M. J. Coleman, A. Chatterjee, and A. Ruina, *Motions of a rimless spoked wheel: A simple 3D system with impacts*, Dynamics and Stability of Systems, 12 (1997), pp. 139–160.

[16] S. Collins, A. Ruina, R. Tedrake, and M. Wisse, *Efficient bipedal robots based on passive dynamic walkers*, Science, 307 (2005), pp. 1082–1085.

[17] C. A. Coulomb, *Théorie des machines simples, en ayant égard au frottement de leur partie, et a la raideur des cordages, avec 5 planches*, Recueil des savants étrangers de l'Académie Royale des Sciences, 10 (1781), pp. 161–332.

[18] C. Canudas de Wit, *On the concept of virtual constraints as a tool for walking robot control and balancing*, Annual Reviews in Control, 28 (2004), pp. 157–166.

[19] S. L. Delp, F. C. Anderson, A. S. Arnold, P. Loan, A. Habib, C. T. John, E. Guendelman, and D. G. Thelen, *Opensim: Open-source software to create and analyze dynamic simulations of movement*, IEEE Transactions on Biomedical Engineering, 54 (2007), pp. 1940–1950.

[20] M. H. Dickinson, C. T. Farley, R. J. Full, M. A. R. Koehl, R. Kram, and S. Lehman, *How animals move: an integrative view*, Science, 288 (2000), pp. 100–106.

[21] A. Esquenazi, M. Talaty, A. Packel, and M. Saulino, *The ReWalk powered exoskeleton to restore ambulatory function to individuals with thoracic-level motor-complete spinal cord injury*, American Journal of Physical Medicine and Rehabilitation, 91 (2012), pp. 911–921.

[22] C. D. Fitzgibbon, *Why do hunting cheetahs prefer male gazelles?*, Animal Behaviour, 40 (1990), pp. 837–845.

[23] L. B. Freidovich, A. S. Shiriaev, and I. R. Manchester, *Stability analysis and control design for an underactuated walking robot via computation of a transverse linearization*, in Proceeding of the 17th IFAC World Congress, 2008, pp. 10166–10171.

[24] R. J. Full and D. Koditschek, *Templates and anchors: Neuromechanical hypotheses of legged locomotion on land*, Journal of Experimental Biology, 202 (1999), pp. 3325–3332.

[25] B. Gamus and Y. Or, *Analysis of dynamic bipedal robot locomotion with stick-slip transitions*, in Proceedings of IEEE International Conference on Robotics and Automation, 2013, pp. 3333–3340.

[26] M. Garcia, A. Chatterjee, and A. Ruina, *Efficiency, speed, and scaling of two-dimensional passive-dynamic walking*, Dynamics and Stability of Sytems, 15 (2000), pp. 75–99.

[27] M. Garcia, A. Chatterjee, A. Ruina, and M. Coleman, *The simplest walking model: Stability, complexity and scaling*, ASME Journal of Biomechanical Engineering, 120 (1998), pp. 281–288.

[28] R. Goebel, R. G. Sanfelice, and A. R. Teel, *Hybrid dynamical systems*, IEEE Control Systems Magazine, 29 (2009), pp. 28–93.

[29] A. T. Goswami, *A study of the passive gait of a compass-like biped robot: Symmetry and chaos*, International Journal of Robotics Research, 17 (1998), pp. 1282–1301.

[30] R. D. Gregg and M. W. Spong, *Reduction-based control of three-dimensional bipedal walking robots*, International Journal of Robotics Research, 29 (2010), pp. 680–702.

[31] J. W. Grizzle, C. Chevallereau, A. D. Ames, and R. Sinnet, *3D bipedal robotic walking: Models, feedback control, and open problems*, in Proc. 8th IFAC Symposium on Nonlinear Control Systems (NOLCOS), 2010, pp. 505–532.

[32] M. Gruhn, O. Hofmann, M. Duebbert, H. Scharstein, and A. Bueschges, *Tethered stick insect walking: A modified slippery surface setup with optomotor stimulation and electrical monitoring of tarsal contact*, J. Neurosci. Methods, 158 (2006), pp. 195–206.

[33] M. Gruhn, L. Zehl, and A. Bueschges, *Straight walking and turning on the slippery surface*, J. Exp. Biol., 212 (2009), pp. 194–209.

[34] J. Guckenheimer and P. Holmes, *Nonlinear Oscillations, Dynamical Systems, and Bifurcations of Vector Fields*, Springer-Verlag, New York, 1983.

[35] H. Hemami and Y.-F. Zheng, *Dynamics and control of motion on the ground and in the air with application to biped robots*, Journal of Robotic Systems, 1 (1984), pp. 101–116.

[36] K. Hirai, M. Hirose, Y. Haikawa, and T. Takenaka, *The development of Honda humanoid robot*, in IEEE Int. Conf. on Robotics and Automation, 1998, pp. 1321–1326.

[37] P. Holmes, R. J. Full, D. Koditschek, and J. Guckenheimer, *The dynamics of legged locomotion: Models, analysis and challenges*, SIAM Review, 48 (2006), pp. 207–304.

[38] Y. Hurmuzlu, F. Génot, and B. Brogliato, *Modeling, stability and control of biped robots—a general framework*, Automatica, 40 (2004), pp. 1647–1664.

[39] S. Kajita, K. Kaneko, K. Harada, F. Kanehiro, K. Fujiwara, and H. Hirukawa, *Biped walking on a low friction floor*, in IEEE/RSJ Conf. on Intelligent Robots and Systems (IROS), 2004, pp. 3546–3552.

[40] K. Kaneko, K K. Harada, F. Kanehiro, G. Miyamori, and K. Akachi, *Humanoid robot HRP-3*, in IEEE/RSJ Conf. on Intelligent Robots and Systems (IROS), 2008, pp. 2471–

2478.
[41] K. Kaneko, F. Kanehiro, S. Kajita, M. Morisawa, K. Fujiwara, K. Harada, and H. Hirukawa, *Slip observer for walking on a low friction floor*, in IEEE/RSJ Conf. on Intelligent Robots and Systems (IROS), 2005, pp. 634–640.
[42] K. Kato and S. Hirose, *Development of the quadruped walking robot, TITAN-IX — mechanical design concept and application for the humanitarian de-mining robot*, Advanced Robotics, 15 (2001), pp. 191–204.
[43] H. K. Khalil, *Nonlinear Systems*, Prentice Hall, second ed., 1996.
[44] E. Krotkov and R. Simmons, *Perception, planning, and control for autonomous walking with the Ambler planetary rover*, International Journal of Robotics Research, 16 (1996), pp. 155–180.
[45] A. D. Kuo, *Energetics of actively powered locomotion using the simplest walking model*, Journal of Biomechanical Engineering, 124 (2002), pp. 113–120.
[46] D. W. Marhefka and D. E. Orin, *Gait planning for energy efficiency in walking machines*, in Proceedings of IEEE International Conference on Robotics and Automation, 1997, pp. 474–480.
[47] M. T. Mason and Y. Wang, *On the inconsistency of rigid-body frictional planar mechanics*, in IEEE Int. Conf. on Robotics and Automation, 1988, pp. 524–528.
[48] T. McGeer, *Passive dynamic walking*, International Journal of Robotics Research, 9 (1990), pp. 62–82.
[49] B. E. Moyer, A. J. Chambers, M. S. Redfern, and R. Cham, *Falls, injuries due to falls, and the risk of admission to a nursing home*, New England Journal of Medicine, 337 (1997), pp. 1279–1284.
[50] ———, *Gait parameters as predictors of slip severity in younger and older adults*, Ergonomics, 49 (2006), pp. 329–343.
[51] M. P. Murphy, A. Saunders, C. Moreira, A. A. Rizzi, and M. Raibert, *The LittleDog robot*, International Journal of Robotics Research, 30 (2011), pp. 145–149.
[52] R. M. Murray, Z. Li, and S. Sastry, *A Mathematical Introduction to Robotic Manipulation*, CRC Press, 1993.
[53] T. Nomura, K. Kawa, Y. Suzuki, M. Nakanishi, and T. Yamasaki, *Dynamic stability and phase resetting during biped gait*, Chaos, 19 (2009), p. 026103.
[54] Y. Or, *Painlevé's paradox and dynamic jamming in simple models of passive dynamic walking*, Regular and Chaotic Dynamics, 19 (2014), pp. 64–80.
[55] Y. Or and A. D. Ames, *Stability and completion of Zeno equilibria in Lagrangian hybrid systems*, IEEE Transactions on Automatic Control, 56 (2011), pp. 1322–1336.
[56] Y. Or and E. Rimon, *Computation and graphical characterization of robust multiple-contact postures in two-dimensional gravitational environments*, Int. J. of Robotics Research, 25 (2006), pp. 1071–1086.
[57] ———, *Investigation of Painlevé's paradox and dynamic jamming during mechanism sliding motion*, Nonlinear Dynamics, 67 (2012), pp. 1647–1668.
[58] Y. Or and A. R. Teel, *Zeno stability of the set-valued bouncing ball*, IEEE Transactions on Automatic Control, 56 (2011), pp. 447–452.
[59] P. Painlevé, *Sur les lois du frottement de glissement*, Comptes Rendus De L'Acadamie Des Sciences, (1895), pp. 112–115.
[60] J.-S. Pang and J. C. Trinkle, *Complementarity formulations and existence of solutions of dynamic multi-rigid-body contact problems with Coulomb friction*, Mathematical programming, 73 (1996), pp. 199–226.
[61] F. Pfeiffer and C. Glocker, *Multibody Dynamics with Unilateral Contacts*, John Wiley & Sons, New York, 1996.
[62] M. Raibert, K. Blankespoor, G. Nelson, R. Playter, and the Bigdog Team, *BigDog, the rough-terrain quadruped robot*, in Proceeding of the 17th IFAC World Congress, 2008, pp. 10822–10825.
[63] E. Rimon, R. Mason, J. W. Burdick, and Y. Or, *A general stance stability test based on stratified morse theory with application to quasi-static locomotion planning*, IEEE Transactions on Robotics, 24 (2008), pp. 626–641.
[64] A. Ruina, J. E. A. Bertram, and M. Srinivasan, *A collisional model of the energetic cost of support work qualitatively explains leg sequencing in walking and galloping, pseudo-elastic leg behavior in running and the walk-to-run transition*, Journal of Theoretical Biology, 237 (2005), pp. 170–192.
[65] U. Saranli, M. Buehler, and D.E. Koditschek, *RHex: a simple and highly mobile hexapod robot*, Int. J. of Robotics Research, 20 (2001), pp. 616 – 631.
[66] J. Schmitt and P. Holmes, *Mechanical models for insect locomotion: dynamics and stability*

in the horizontal plane - I. theory, Biological Cybernetics, 83 (2000), pp. 501–515.
[67] J. Seipel and P. Holmes, *A simple model for clock-actuated legged locomotion*, Regular and Chaotic Dynamics, 12 (2007), pp. 502–520.
[68] M. Sheen, B. Kogan, J. Hasaneini, and A. Ruina, *Evaluating simulation tools for use in walking robot design and controls optimization*, in Dynamic Walking, Zurich, Switzerland, June 2014.
[69] F. M. Silva and J. A. T. Machado, *Energy analysis during biped walking*, in Proceedings of IEEE International Conference on Robotics and Automation, 1999, pp. 59–64.
[70] J. A. Smith, I. Sharf, and M. Trentini, *PAW: a hybrid wheeled-leg robot*, in Proceedings of IEEE International Conference on Robotics and Automation, 2006, pp. 4043–4048.
[71] R. Smithers, *The mammals of Botswana*, National Musuems of Rhodesia, 1971.
[72] A. Spence, K. Parsons, M. Ferrari, T. Pfau, A. Wilson, and A. Thurman, *Effects of substrate properties on equine locomotion*, Comparative Biochemistry and Physiology A-Molecular and Integrative Physiology, 146 (2007), pp. Suppl. A6.8:S109–S109.
[73] M. W. Spong and F. Bullo, *Controlled symmetries and passive walking*, IEEE Trans. on Automatic Control, 50 (2005), pp. 1025–1031.
[74] M. W. Spong, J. K. Holm, and D. Lee, *Passivity-based control of bipedal locomotion*, IEEE Robotics & Automation Magazine, 14 (2007), pp. 30–40.
[75] L. Strandberg and H. Lanshammar, *The dynamics of slipping accidents*, Journal of Occupational Accidents, 3 (1981), pp. 153–162.
[76] W. J. Stronge, *Impact Mechanics*, Cambridge University Press, Cambridge, UK, 1979.
[77] N. Suzuki and Y. Yamamoto, *Pursuing entertainment aspects of SONY AIBO quadruped robots*, in 4th International Conference on Modeling, Simulation and Applied Optimization (ICMSAO), 2011, pp. 1–5.
[78] A. Tavakoli and Y. Hurmuzlu, *Robotic locomotion of three generations of a family tree of dynamical systems, part I: Passive gait patterns*, Nonlinear Dynamics, 73 (2013), pp. 1969–1989.
[79] J. A. Vazquez and M. Velasco-Villa, *Numerical analysis of the sliding effects of a 5-dof biped robot*, in 8th International Conference on Electrical Engineering Computing Science and Automatic Control, 2011, pp. 1–6.
[80] ———, *Experimental estimation of slipping in the supporting point of a biped robot*, Journal of Applied Research and Technology, 11 (2013), pp. 348–359.
[81] Y. Wang and M. T. Mason, *Two-dimensional rigid body collisions with friction*, J. of Applied Mechanics, 10 (1993), pp. 292–352.
[82] E. R. Westervelt, J. W. Grizzle, C. Chevallereau, J. H. Choi, and B. Morris, *Feedback Control of Dynamic Bipedal Robot Locomotion*, CRC Press, 2007.
[83] E. R. Westervelt, J. W. Grizzle, and D. E. Koditschek, *Hybrid zero dynamics of planar biped walkers*, IEEE Trans. on Automatic Control, 48 (2003), pp. 42–56.
[84] B. H. Wilcox, T. Litwin, J. Biesiadecki, J. Matthews, M. Heverly, J. Morrison, J. Townsend, N. Ahmed, A. Sirota, and B. Cooper, *ATHLETE: A cargo handling and manipulation robot for the moon*, Journal of Field Robotics, 24 (2007), pp. 421–434.
[85] D. Zarrouk and R. S. Fearing, *Cost of locomotion of a dynamic hexapedal robot*, in Proceedings of IEEE International Conference on Robotics and Automation, 2013, pp. 2533–2538.
[86] J. Zhang, K. H. Johansson, J. Lygeros, and S. Sastry, *Zeno hybrid systems*, International Journal of Robust and Nonlinear Control, 11 (2001), pp. 435–451.
[87] Supplementary movie files are submitted online along with the manuscript.